The influence of shear-dependent rheology on turbulent pipe flow

J. Singh[1], M. Rudman[1,†] and H. M. Blackburn[1]

[1]Department of Mechanical and Aerospace Engineering, Monash University, VIC 3800, Australia

Direct numerical simulations of turbulent pipe flow of power-law fluids at $Re_\tau = 323$ are analysed in order to understand the way in which shear thinning or thickening affects first- and second-order flow statistics including turbulent kinetic energy production, transport and dissipation in such flows. The results show that with shear thinning, near-wall streaks become weaker and the axial and azimuthal correlation lengths of axial velocity fluctuations increase. Viscosity fluctuations give rise to an additional shear stress term in the mean momentum equation which is negative for shear-thinning fluids and which increases in magnitude as the fluid becomes more shear thinning: for an equal mean wall shear stress, this term increases the mean velocity gradient in shear-thinning fluids when compared to a Newtonian fluid. Consequently, the mean velocity profile in power-law fluids deviates from the law of the wall $U_z^+ = y^+$ in the viscous sublayer when traditional near-wall scaling is used. Consideration is briefly given to an alternative scaling that allows the law of wall to be recovered but which results in loss of a common mean stress profile. With shear thinning, the mean viscosity increases slightly at the wall and its profile appears to be approximately logarithmic in the velocity log layer. Through analysis of the turbulent kinetic energy budget, undertaken here for the first time for generalised Newtonian fluids, it is shown that shear thinning decreases the overall turbulent kinetic energy production but widens the wall-normal region where it is generated. Additional dissipation terms in the mean flow and turbulent kinetic energy budget equations arise from viscosity fluctuations; with shear thinning, these result in a net decrease in the total viscous dissipation. The overall effect of shear thinning on the turbulent kinetic energy budget is found to be largely confined to the inner layers, $y^+ \lesssim 60$.

Key words: non-Newtonian flows, pipe flow boundary layer, turbulent flows

---

1. Introduction

Many fluids do not display constant viscosity and are known as non-Newtonian fluids. They are important in many practical applications. Generalised Newtonian (GN) fluids are a class of non-Newtonian fluids in which the fluid stress is proportional to the local instantaneous strain rate via a non-uniform viscosity,

$$\boldsymbol{\tau}(\boldsymbol{r}, t) = 2\rho\nu(\boldsymbol{r}, t)\boldsymbol{s}(\boldsymbol{r}, t). \tag{1.1}$$

† Email address for correspondence: murray.rudman@monash.edu

Here, $\boldsymbol{\tau}$ is the stress tensor, ρ is density, ν is fluid kinematic viscosity and $\boldsymbol{s}$ is the strain rate $\boldsymbol{s} = [\nabla\boldsymbol{v} + (\nabla\boldsymbol{v})^{\mathrm{T}}]/2$ where T represents the matrix transpose. In (1.1) $\boldsymbol{r}$ is the position vector and t is time. For GN fluids, the fluid viscosity is typically defined as being a function of the strain rate, $\nu = \nu(\dot{\gamma})$ where $\dot{\gamma} = (2\boldsymbol{s} : \boldsymbol{s})^{1/2}$, the second invariant of the strain-rate tensor. The GN assumption implies that flows are free from elastic effects and that the response of the fluid to an applied shear stress is instantaneous. Fine particle suspensions, paints and food products such as molten chocolate, mayonnaise and tomato ketchup, are examples of GN fluids. GN fluids can be broadly categorised based on whether or not they show a yield stress i.e. the minimum shear stress required before the fluid starts to shear. In this study, we only consider fluids which do not show a yield stress.

The rheology of a GN fluid is determined experimentally using a rheogram (i.e. shear stress versus shear-rate data). Typically, a particular rheological model is fitted to the rheogram via regression. Model parameters determined via such regressions have no intrinsic physical meaning, but nevertheless are very useful in predicting flow behaviour and are extensively used. There are many rheology models available for GN fluids (see e.g. Chhabra & Richardson 2008) but for GN fluids which do not show a yield stress, in particular for shear-thinning fluids, a power-law (PL) rheology model is commonly used, despite having an infinite zero-shear viscosity that is not observed in practice. Such fluids are the focus of the present work. The PL rheology model defines the fluid viscosity as:

$$\nu = \rho^{-1} K \dot{\gamma}^{n-1}, \tag{1.2}$$

where the consistency K and flow index n are model parameters. The PL rheology model describes shear-thinning behaviour when $0 < n < 1$, i.e. the viscosity of the fluid decreases with increase in shear rate, and for $n > 1$ shear-thickening behaviour.

The non-uniform viscosity of PL fluids makes the choice of an appropriate viscosity scale (and hence Reynolds number) unclear. Instead of defining a viscosity scale, Metzner & Reed (1955) proposed the following definition of Reynolds number (now known as the Metzner–Reed Reynolds number) for PL fluids by collapsing laminar flow friction factor data on to the Newtonian curve:

$$Re_{MR} = \frac{8\rho U_b^{2-n} D^n}{K(6 + 2/n)^n}, \tag{1.3}$$

where D is pipe diameter and U_b is the bulk velocity (flow rate per unit area). This definition is widely used, although it may be argued that it is not appropriate for turbulent flows because it is derived from a laminar flow analysis (Guzel, Frigaard & Martinez 2009). Additionally, turbulent flow of PL fluids with different n but the same Re_{MR} can show significantly different turbulent flow behaviour (Rudman *et al.* 2004).

Another Reynolds number commonly used for GN fluids is based on the nominal wall viscosity ν_w (Pinho & Whitelaw 1990; Ptasinski *et al.* 2001; Pinho 2003; Rudman *et al.* 2004). For a PL fluid it is easily shown using the mean wall shear stress τ_w and (1.2) that

$$\nu_w = \rho^{-1} K^{1/n} \tau_w^{(1-1/n)}, \tag{1.4}$$

where τ_w is determined from the mean pressure gradient in the axial (z) direction $\partial P/\partial z$ as $\tau_w = (D/4)\partial P/\partial z$. Using this viscosity scale, a generalised bulk Reynolds number Re_G and a friction Reynolds number Re_τ are defined as

$$Re_G = U_b D/\nu_w \quad \text{and} \quad Re_\tau = u^* R/\nu_w, \tag{1.5a,b}$$

where $R = D/2$ is pipe radius and $u^* = (\tau_w/\rho)^{1/2}$ is the friction velocity. Other definitions of Reynolds number have been proposed (Tomita 1959; Clapp 1961; Slatter & Lazarus 1993; Chilton & Stainsby 1998; Madlener, Frey & Ciezki 2009; Guzel *et al.* 2009), however there is no clear evidence to suggest that one definition is more useful than others in describing and collapsing data from turbulent flows of GN fluids. We adopt (1.4) and (1.5) in the present work.

Computational modelling of GN fluids, especially using direct numerical simulation (DNS), shows promise in helping to understand transition and turbulence in these fluids. The main benefit of using DNS is that once validated, it can be reliably used to model flow behaviour and provide a detailed picture of turbulence structure that is almost impossible to obtain in real GN fluids, which are usually opaque. DNS has the added benefit that rheological effects such as viscoelasticity (often unintentionally present, although small, in physical experiments using model GN fluids) can be excluded and the effect of modifying individual rheological parameters can be readily isolated. Additionally, the technique allows the validity of rheological models to be assessed in different flow scenarios.

DNS of GN fluids was first presented by Rudman *et al.* (2004) and Rudman & Blackburn (2006), results of which showed that in a turbulent pipe flow, shear thinning reduced the friction factor (technically equivalent to drag reduction) at a given Re_G. Transition to turbulence, quantified by transition Re_G, was also delayed by shear thinning, which was also in agreement with experimental results of Pinho & Whitelaw (1990) and Rudman *et al.* (2002). The maximum Reynolds number in those studies was $Re_G \approx 8000$, however, the flow was weakly turbulent for the moderately shear-thinning fluid ($n = 0.69$) considered there. Additionally there were significant discrepancies between the results from DNS and experiments as discussed in Rudman & Blackburn (2006). These discrepancies have recently been shown to be caused by a lack of high shear-rate data used in rheology characterisation (Singh *et al.* 2016). Local, instantaneous shear rates in turbulent pipe flow, especially near the wall, can be much higher (by an order of magnitude) than the maximum shear rate commonly used in rheology characterisation. Use of low-shear rheology in DNS implicitly involves extrapolating the rheology far outside the shear-rate range over which it is measured, leading to erroneous results. Hence, reliable high-shear rheology data are essential in matching DNS and experimental studies of turbulent flows of GN fluids. The other DNS study of PL fluids is by Gavrilov & Rudyak (2016) at relatively higher Re_G (10 000 and 20 000) which observed similar results as reported by Rudman *et al.* (2004) and Rudman & Blackburn (2006). Gavrilov & Rudyak (2016) proposed that shear thinning decreases the turbulent energy transfer from the axial component to others which leads to an increased anisotropy compared to a Newtonian fluid.

Other computational (though not DNS) studies of the turbulent flow of GN fluids are represented by Malin (1997), Cruz & Pinho (2003), Ohta & Miyashita (2014) and Gnambode *et al.* (2015). Gnambode *et al.* (2015) used large eddy simulation (LES) to examine the effect of GN rheology on the turbulence flow whereas the others developed Reynolds-averaged Navier–Stokes (RANS) or LES models for GN fluids.

There is a paucity of DNS results for even first-order flow statistics, which is a gap that needs to be filled in order to understand and correctly model turbulent transport of momentum in these fluids. To overcome the limited Re_G in Rudman *et al.* (2004) and Rudman & Blackburn (2006), the current study considers flow at a higher Reynolds number ($Re_G \approx 12\,000$, $Re_\tau = 323$). The effects of shear thinning and shear thickening on turbulent pipe flow are considered and profiles of mean flow, turbulence

intensities and budgets of mean shear stress and mean and turbulent kinetic energies are investigated.

To our knowledge the present work is the first study of these budgets in turbulent pipe flow of a GN fluid. The key finding is that the effect of PL rheology on turbulent pipe flow is mainly significant in the inner, near-wall layers.

2. Mathematical formulation

2.1. *Governing equations*

Here, we briefly review the simulation methodology, and refer the reader to Blackburn & Sherwin (2004) and Rudman & Blackburn (2006) for more detailed descriptions. Since the instantaneous viscosity is spatially varying, the incompressible Navier–Stokes equations must be written in stress-divergence form:

$$\mathrm{D}\boldsymbol{v}/\mathrm{D}t = \rho^{-1}(-\boldsymbol{\nabla}p + \boldsymbol{\nabla} \cdot \boldsymbol{\tau} + \rho\boldsymbol{g}), \quad \text{with } \boldsymbol{\nabla} \cdot \boldsymbol{v} = 0, \qquad (2.1)$$

where $\boldsymbol{v}$ is the velocity vector, p is the static pressure, $\boldsymbol{\tau}$ is the stress tensor and $\rho\boldsymbol{g}$ is the body force. For ease of notation, we will divide p, $\boldsymbol{\tau}$ and $\rho\boldsymbol{g}$ in (2.1) by the constant fluid density ρ, but refer to them as pressure, stress and body force respectively. The stress tensor $\boldsymbol{\tau}$ is modelled with the GN assumption as:

$$\boldsymbol{\tau} = 2\nu(\dot{\gamma})\boldsymbol{s}, \qquad (2.2)$$

where $\boldsymbol{s}$ is the instantaneous strain-rate tensor and the kinematic viscosity ν is calculated using the PL model (see (1.2)). The numerically singular viscosity of PL rheology model at zero shear rate is avoided by using a 'cutoff' value below which the shear rate is assumed constant for calculating the viscosity. A very low value for the shear-rate cutoff (1×10^{-6}) is used to ensure that it does not affect the flow predictions: no shear rate in the present work reaches such a low value.

For numerical robustness, the convective term in (2.1) is implemented in skew-symmetric form, i.e. $(\boldsymbol{v} \cdot \boldsymbol{\nabla}\boldsymbol{v} + \boldsymbol{\nabla} \cdot \boldsymbol{v}\boldsymbol{v})/2$. The axial pressure gradient is applied as a body force term via $\boldsymbol{g}$ in (2.1). The form of the Navier–Stokes equations implemented in the code is written as:

$$\partial\boldsymbol{v}/\partial t + (\boldsymbol{v} \cdot \boldsymbol{\nabla}\boldsymbol{v} + \boldsymbol{\nabla} \cdot \boldsymbol{v}\boldsymbol{v})/2 = -\boldsymbol{\nabla}p + \boldsymbol{\nabla} \cdot (2\nu\boldsymbol{s}) + \boldsymbol{g}. \qquad (2.3)$$

The spatial discretisation uses two-dimensional spectral elements to cover the pipe cross-section as shown in figure 1 and Fourier expansion in the axial (z) direction. The spectral element representation uses standard tensor-product nodal basis with Gauss–Lobatto–Legendre collocation points. The body force acts only in the axial direction giving $g = g_z$ which is set to achieve a desired flow rate, g takes the place of an axial pressure gradient and thus the pressure in (2.3) can be periodic as required by the Fourier expansion used in this direction. Execution is parallel over planar Fourier modes; product terms are computed pseudo-spectrally and not de-aliased. Time integration is second order and uses backwards differencing for approximating temporal derivatives in the velocity correction scheme (Karniadakis, Israeli & Orszag 1991; Guermond, Minev & Shen 2006). The time integration method as originally proposed by Karniadakis *et al.* (1991) requires a spatially constant viscosity which is accommodated here by adopting a technique introduced by Leslie & Gao (1988) in the context of LES. The viscosity ν is split into a spatially constant component, ν_{ref}, with variable remainder $\nu - \nu_{ref}$ to give the momentum equation

$$\partial\boldsymbol{v}/\partial t + (\boldsymbol{v} \cdot \boldsymbol{\nabla}\boldsymbol{v} + \boldsymbol{\nabla} \cdot \boldsymbol{v}\boldsymbol{v})/2 = -\boldsymbol{\nabla}p + \nu_{ref}\nabla^2\boldsymbol{v} + 2\boldsymbol{\nabla} \cdot \{(\nu - \nu_{ref})\boldsymbol{s}\} + \boldsymbol{g}. \qquad (2.4)$$
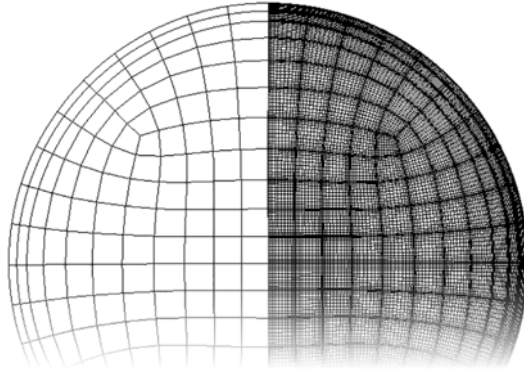
FIGURE 1. Detail of a spectral element mesh used to discretise the pipe cross-section for $n = 0.4$–1.2, illustrating the elements (left) and grid nodes for twelfth-order element interpolation functions, $N_p = 12$ (right). The mesh used for $n = 1.2$ was slightly finer and had more elements near the pipe centre.

Following this decomposition, the term $\nu_{ref}\nabla^2 \boldsymbol{v}$ is handled implicitly in time, while the remaining viscous term is dealt with explicitly and grouped with the nonlinear terms. One advantage of this method is that by appropriate choice of ν_{ref}, it is possible to integrate stably with time steps close to the Courant–Friedrichs–Lewy limit, rather than at smaller values which would be determined by a fully explicit treatment of viscous diffusion.

2.2. *Reynolds-averaged Navier–Stokes equation for an incompressible GN fluid*

Reynolds decomposition is used to separate variables into their ensemble mean and the fluctuating components. Here, the velocity is decomposed as $\boldsymbol{v} = \boldsymbol{V} + \boldsymbol{v}'$; viscosity $\nu = \bar{\nu} + \nu'$ and the rate of strain tensor as $\boldsymbol{s} = \boldsymbol{S} + \boldsymbol{s}'$, where $\boldsymbol{V}$, $\bar{\nu}$ and $\boldsymbol{S}$ are the time-averaged quantities. Important to note for subsequent discussion is that $\bar{\nu}_w \neq \nu_w$, as shown later in §4.1. Thus the Reynolds-averaged mean momentum equation for an incompressible non-Newtonian fluid is written as:

$$\boldsymbol{V} \cdot \nabla \boldsymbol{V} = -\nabla P + \nabla \cdot \overline{\boldsymbol{\tau}} + \boldsymbol{g}. \quad (2.5)$$

In (2.5), the mean stress tensor is the sum of three stress components.

$$\begin{aligned} \overline{\boldsymbol{\tau}} &= 2\bar{\nu}\boldsymbol{S} - \overline{\boldsymbol{v}'\boldsymbol{v}'} + 2\overline{\nu'\boldsymbol{s}'} \\ &= \boldsymbol{\tau}^v + \boldsymbol{\tau}^R + \boldsymbol{\tau}^{fv}. \end{aligned} \quad (2.6)$$

As in the mean momentum equation for a Newtonian fluid, there is a mean viscous stress ($\boldsymbol{\tau}^v$) and a Reynolds stress ($\boldsymbol{\tau}^R$). For GN fluids a new stress term arises ($\boldsymbol{\tau}^{fv}$) which we call the turbulent viscous stress ($\boldsymbol{\tau}^{fv}$). In the literature for viscoelastic fluids, an equivalent term is referred to as the 'polymer stress' (Ptasinski *et al.* 2001). The terminology is not appropriate here as its contribution to the mean stress is not related to polymer addition to a carrier fluid and will be shown to have a different character to the same term in viscoelastic fluids. Unlike other stress terms, $\boldsymbol{\tau}^{fv}$ can be positive or negative depending on the rheology of the fluid and unlike $\boldsymbol{\tau}^R$, it does not vanish at the wall. This is because it is a correlation between the fluctuations in viscosity

$\nu' = \nu - \bar{\nu}$ and shear rate $s' = s - S$. Both mean and fluctuating shear rates are non-zero at the wall because they are related to velocity gradients that do not vanish there. Similarly, viscosity and its fluctuations are non-zero at the wall as they depend on shear rate there. Therefore, we do not expect the correlation τ^{fv} to vanish at the wall. Using an order of magnitude analysis, Pinho (2003) showed that τ^{fv} could only be neglected in the mean flow of a non- or weakly shear-thinning fluid and for strongly shear-thinning fluids, especially in the vicinity of the wall, this term can be large. The other difference in (2.5) compared to its Newtonian version is that the mean viscous stress is formed from a spatially varying viscosity, $\bar{\nu}(r)$.

2.3. *Non-dimensional variables*

For most of the analysis below, wall units are defined in a similar manner to the Newtonian analysis using the nominal wall viscosity ν_w (1.4) as the viscosity scale. The friction velocity $u^* = (\tau_w/\rho)^{1/2}$ is used for the velocity scale and ν_w/u^* for the length scale. Hence, the distance from the wall is expressed as $y^+ = (R - r)/(\nu_w/u^*)$, where r is the radial distance from the centre of the pipe. The non-dimensional mean axial velocity and mean viscosity are expressed as $U_z^+ = U_z/u^*$ and $\nu^+ = \bar{\nu}/\nu_w$. Turbulence intensities are expressed in wall units as $u_i'^+ = (\overline{u_i'^2})^{1/2}/u^*$. Shear rate is normalised by u^{*2}/ν_w, stress terms by ρu^{*2} and the energy budget terms by $(u^*)^4/\nu_w$. The Fanning friction factor, f, which is the non-dimensional wall shear stress, is defined as $f = 2\tau_w/(\rho U_b^2)$.

Although the mean wall shear stress, τ_w, and the nominal wall viscosity, ν_w, are chosen here for scaling, it is shown later in § 4.3 that these scalings do not maintain the fundamental $U_z^+ = y^+$ relation near the wall. Later we will develop a scaling that gives $U_z^+ = y^+$, however, we choose to use ν_w and u^* in the majority of the analysis below because these can be determined *a priori* from the mean pressure gradient which is easily measured in experiments. This allows a direct comparison to DNS results.

2.4. *Simulation parameters*

In the present study, DNS are run for flow indices in the range $n = 0.4$–1.2. The governing equation (2.4) is non-dimensionalised by the friction velocity and the pipe radius $R = 0.5$. This non-dimensionalisation gives $\nu_w = 1/Re_\tau$ and the non-dimensional body force $gR/u^{*2} = 2$. We chose a friction Reynolds number $Re_\tau = 323$ in the current simulations to attain a wider range of length scales in the flow than those previously reported in Rudman *et al.* (2004). The consistency K for a given n is calculated using the expression of the nominal wall viscosity ν_w (1.4). A summary of simulation conditions is given in table 1 and the fluid viscosity normalised by ν_w is plotted against shear rate (viscosity rheogram) in figure 2 for different n. It can be seen that shear thinning affects the viscosity estimates significantly at all shear rates except for $\dot{\gamma} = \tau_w/\nu_w$ ($\dot{\gamma}^+ = 1$) for which the nominal wall viscosity is forced to be the same for all n. The predicted bulk velocity and therefore, generalised Reynolds number Re_G slightly decrease with increasing n.

2.5. *Mesh design*

Mesh design for these flows has been an iterative process, influenced by rules of thumb for the resolution and domain size established in Newtonian DNS (Piomelli 1997); by our previous experience (Rudman *et al.* 2004; Rudman & Blackburn 2006);

n	$K/(\rho u^{*2-n}R^n)$	U_b/u^*	Re_G	Re_{MR}	$f_{DM} \times 10^3$	$f \times 10^3$	Δf (%)	DR (%)
0.4	9.9080×10^{-2}	18.34	11 862	4 291	5.60	5.94	5.0	24
0.6	3.1181×10^{-2}	17.23	11 093	5 498	6.64	6.70	0.9	14
0.8	9.8128×10^{-3}	16.49	10 630	7 401	7.29	7.34	0.6	6
1.0	3.0870×10^{-3}	15.93	10 322	10 322	7.66	7.87	2.0	0
1.2	9.7179×10^{-4}	15.56	10 117	14 786	7.84	8.21	4.0	−4

TABLE 1. Summary of simulation conditions for different flow indices n ($n=1$ represents the Newtonian case). DR (drag reduction) is defined as $(f - f_{Newt})/f_{Newt}$ where f is a Fanning friction factor. Friction Reynolds number Re_τ, non-dimensional body force gR/u^{*2} and therefore the nominal wall viscosity ν_w are fixed at 323, 2 and 1/323 respectively.
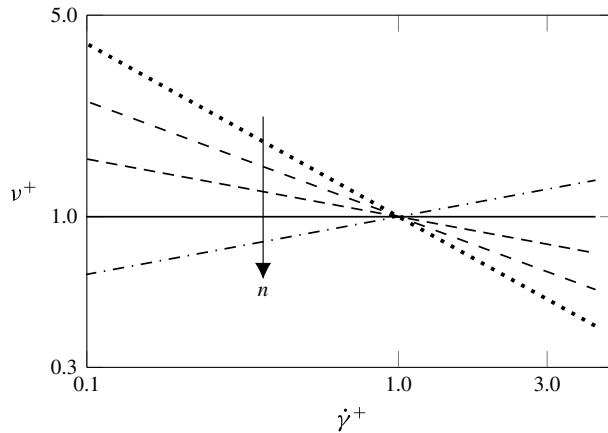
FIGURE 2. Non-dimensionalised viscosity plotted as a function of non-dimensional shear rate for different n (see table 1) on a log–log scale. In this and subsequent figures, arrows labelled n indicate sense of increasing flow index.

and results from preliminary investigations over the range of flow indices investigated. Turbulence structures become finer with decreasing shear thinning (i.e. increasing n). Therefore, DNS requires a higher mesh resolution as n is increased. In case of a shear-thickening fluid, due to the lower viscosity in the core region (and hence turbulent eddies with smaller length scales) a higher mesh resolution is required in the core region compared to a Newtonian simulation at the same Re_τ. In order to ensure mesh convergence for all cases, a grid resolution study was performed for $n = 1.0$ and the same mesh was used for $n = 0.4$–1.0 which implies a more finely resolved mesh for these cases. A separate grid resolution study was conducted for $n = 1.2$. The final meshes used in simulations had 300 spectral elements for $n = 0.4 - 1.0$ and 384 spectral elements for $n = 1.2$. All meshes used twelfth-order tensor-product shape functions and 384 axial data planes giving the near-wall mesh spacing of $y_w^+ = 0.8$ in the wall-normal direction, $(r\Delta\theta)_w^+ = 4.5$ in the azimuthal direction and $\Delta z^+ = 21$ in the axial direction for $n = 0.4$–1.0. The mesh resolution was slightly finer for $n = 1.2$ in the azimuthal direction, $(r\Delta\theta)_w^+ = 3.5$, and near the pipe centre. These near-wall mesh spacings in the wall normal and the azimuthal direction agree with typical values used for wall resolving DNS of Newtonian fluids (Piomelli 1997; Moser, Kim & Mansour 1999; Chin, Monty & Ooi 2014). Although, the mesh in the axial
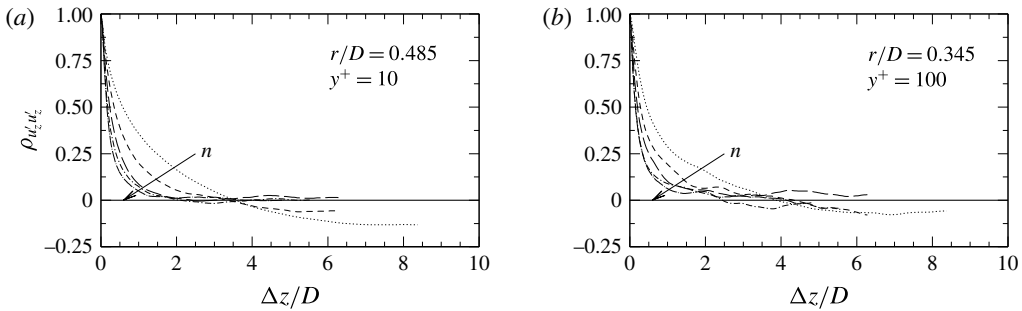
FIGURE 3. Two point correlation coefficient of axial velocity fluctuations as a function of streamwise separation $\Delta z/D$ plotted for different n (see table 1) at two different y^+ locations.

direction is coarser than that used in Newtonian studies (Moser *et al.* 1999; Chin *et al.* 2014), our mesh resolution study showed that further mesh refinement did not change the results noticeably.

2.6. *Domain length independence study*

To ensure that the axial domain periodicity did not unduly influence results, a domain length independence study was carried out. Since the range of length scales in the flow decreases with decreasing n, $n = 0.6$ was chosen for this study. Results showed that a minimum domain length of $11D$ is required in order that streamwise correlations are sufficiently small and the turbulence statistics converge. In the final simulations, a domain length of $L_z = 4\pi D$ is used for $n = 0.6$–1.2 which is twice that used by Eggels *et al.* (1994) in their DNS of a Newtonian fluid at $Re_\tau = 180$ and comparable to that suggested by Chin *et al.* (2010) for DNS of a Newtonian fluid at $Re_\tau = 170$–500. A slightly longer domain ($L_z \approx 16D$) is used for $n = 0.4$ due to its transitional nature (discussed later). These domain lengths are further checked for their adequacy via two point axial correlations of axial velocity fluctuations $\rho_{u'_z u'_z}$ defined as:

$$\rho_{u'_z u'_z}(\Delta z) = \langle u'_z(r, \theta, z, t) u'_z(r, \theta, z + \Delta z, t) \rangle / \langle u'_z(r, \theta, z)^2 \rangle. \tag{2.7}$$

Here, u'_z represents the axial velocity fluctuations at time t and $\langle \rangle$ denotes averaging. As seen in figure 3 $\rho_{u'_z u'_z}$ decays to zero for all n. Close to the centre of the pipe (not shown) $\rho_{u'_z u'_z}$ remains positive for much of the domain, although less than 0.1. Overall, these results indicate adequate domain length. Negative values of $\rho_{u'_z u'_z}$ in the profiles of $n = 0.4$ and $n = 0.6$ indicate intermittent turbulent regions which are also seen in near-wall streaks shown later (in figure 6). The larger negative values of $\rho_{u'_z u'_z}$ for $n = 0.4$ indicate the transitional nature of this flow. Therefore we exclude the results of $n = 0.4$ and present those only for $n = 0.6$–1.2.

2.7. *Temporal averaging*

Initial conditions were taken from earlier simulations on different meshes or from simulations with different n. Simulations were run until the calculated instantaneous total wall shear stress and the bulk velocity had reached a statistically steady value. In most cases the wall shear stress and the bulk velocity fluctuated by approximately
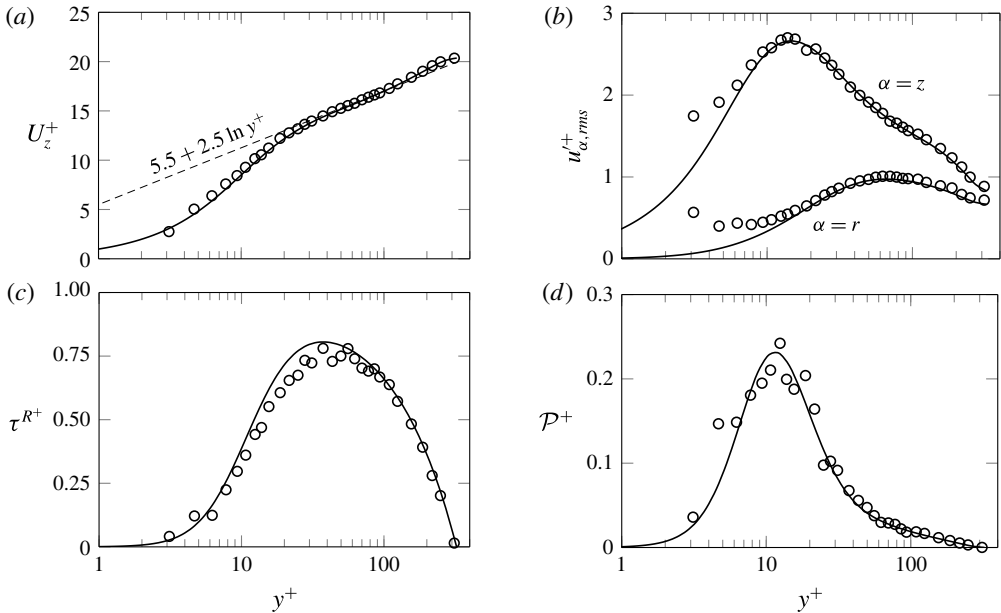
FIGURE 4. Wall scaled statistical profiles from DNS of Newtonian fluid at $Re_\tau = 323$ (solid line), compared to experimental results of den Toonder & Nieuwstadt (1997, circles: $Re_\tau = 314$). (*a*) Mean axial velocity; (*b*) axial and radial turbulence intensities; (*c*) Reynolds shear stress; (*d*) turbulent kinetic energy production.

2 % about the mean value. The time interval required to reach this state typically corresponded to around ten to twenty domain wash-through times. Once this state had been reached, time-averaged statistics were accumulated over another fifteen to twenty transit times.

2.8. *Validation of numerical method*

To provide a baseline comparison of the numerical method, statistical data for turbulent pipe flow of a Newtonian fluid at $Re_\tau = 323$ are compared in figure 4 to the experimental results of den Toonder & Nieuwstadt (1997) obtained by Laser doppler anemometry (LDV) measurement at a similar Re_τ of 314. As seen in the figure, profiles of mean axial velocity, turbulence intensities, Reynolds shear stress and turbulent kinetic energy production obtained from DNS agree well with the experimental results except very close to the wall, where some of the experimental results are acknowledged to be unreliable.

The DNS friction factor predictions for different flow indices are compared with the Dodge and Metzner correlation (Dodge & Metzner 1959) which gives the best agreement with experiments compared to others (Hartnett & Kostic 1990). As seen in table 1, DNS predictions of the friction factor for different flow indices agree well (within 5 %) with the Dodge and Metzner correlation suggesting the accuracy of the current results. Note that the errors in predicting f compared to Dodge and Metzner's correlation is lower in the current study compared to our earlier studies (Rudman *et al.* 2004; Rudman & Blackburn 2006) where the flow was weakly turbulent. Since the Dodge and Metzner correlation is a semi-empirical correlation with the parameters determined using turbulent flow experiments, it is prone to give erroneous prediction
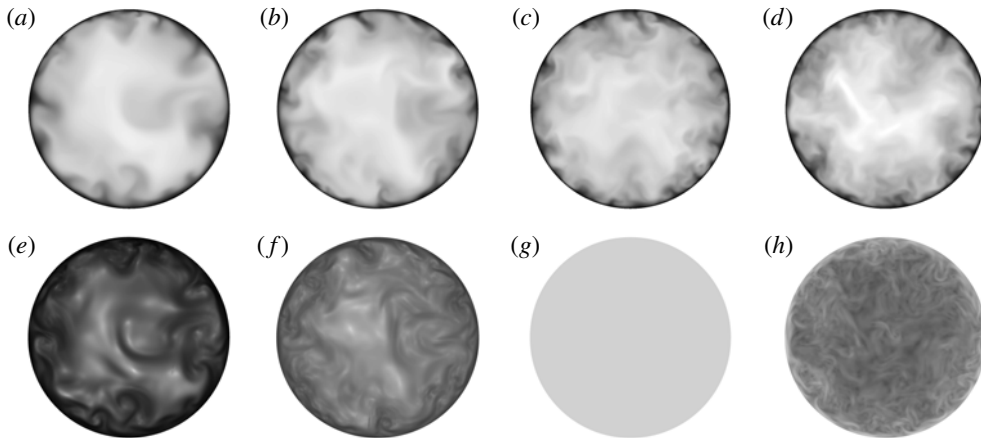
FIGURE 5. (*a–d*) Contours of instantaneous axial velocity normalised by the bulk velocity U_b (0 is black, 1.4 is white). (*e–h*) Contours of instantaneous viscosity normalised by the maximum viscosity (0.1 is black, 1.0 is light grey). From left to right, flow indices are (*a,e*) $n = 0.6$, (*b,f*) $n = 0.8$, (*c,g*) $n = 1.0$ and (*d,h*) $n = 1.2$. The velocity and viscosity contours for a given fluid are plotted for the same time instant.

in weakly turbulent flows. Results presented in Singh *et al.* (2016) also support the validity of the present simulation methodology for GN fluids.

3. Observations of instantaneous flow

The effect of flow index n on instantaneous flow structures is shown in figures 5 and 6. Finer-scale structure is observed with increasing n, which is seen clearly in the contours of axial velocity and viscosity plotted on a pipe cross-section in figure 5 and in the near-wall streaks shown in figure 6. The finer scales also correspond to higher frequency motions, although later it will be seen they are also associated with lower turbulent kinetic energy. The longer, wider low-speed streaks seen in figure 6 for lower n are associated with reduced wall-normal turbulence intensities by shear thinning which will be discussed in §4.4. There are qualitative correlations evident between the surface contours on adjacent surfaces indicating the radial extent of these structures, which indicate the imprint of the outer flow on near-wall fluctuations (Hutchins & Marusic 2007).

The information presented in figure 6 can be quantified using the velocity integral length scale which is a measure of the characteristic correlation distance between the velocity fluctuations at two points in the flow field. Here, the streamwise velocity integral length scale, l_z, is calculated by integrating the two point autocorrelation function (2.7) to the point where it first crosses zero. As expected from the qualitative information in figure 6, l_z increases with decreasing n (figure 7*a,b*) from approximately 60 for $n = 1$ to around 100 for $n = 0.6$. This suggests that axial velocity fluctuations are correlated for a longer distance for lower n. For all flow indices, the maximum l_z occurs at $y^+ \approx 10$ with the exact location slightly shifting away from the wall with decreasing n (figure 7*b*). Azimuthal length scales near the pipe wall follow a similar trend with n (figure 7*c*).
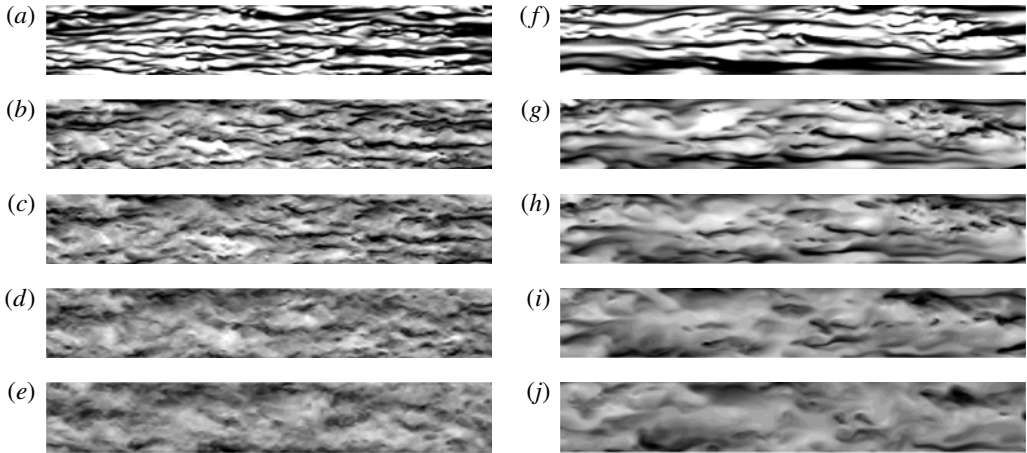
FIGURE 6. Contours of instantaneous axial velocity fluctuations normalised by the local mean axial velocity at $y^+ = 10, 30, 45, 70, 100$ (from top to bottom) for (*a–e*) Newtonian and (*f–j*) $n = 0.6$ plotted on surfaces of constant y^+. White represents positive fluctuation and black negative. Contours have been stretched azimuthally to maintain the same vertical extent.
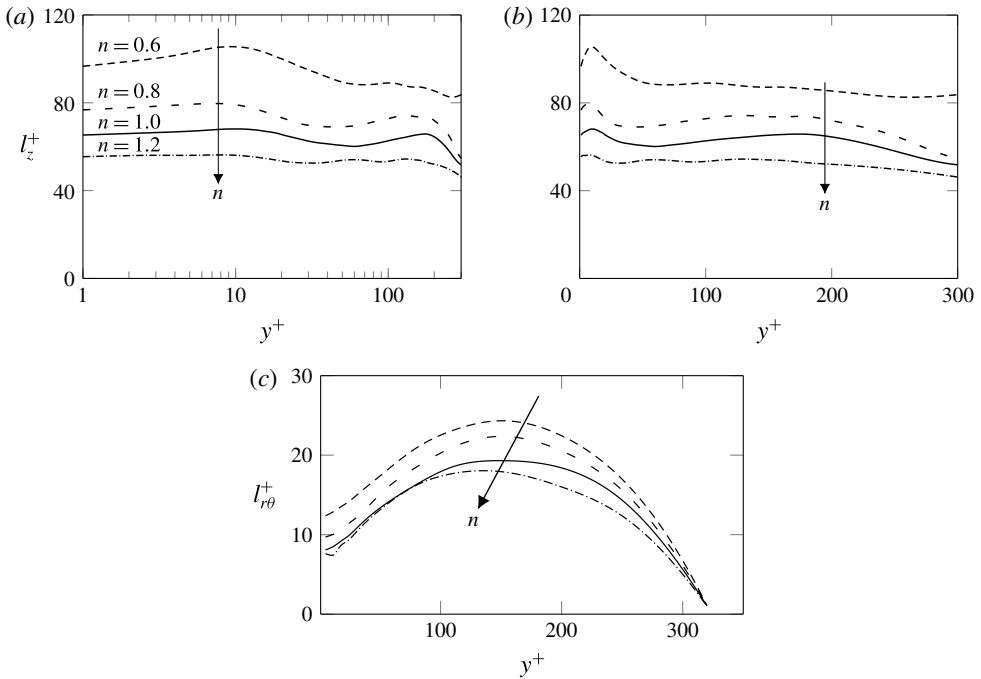

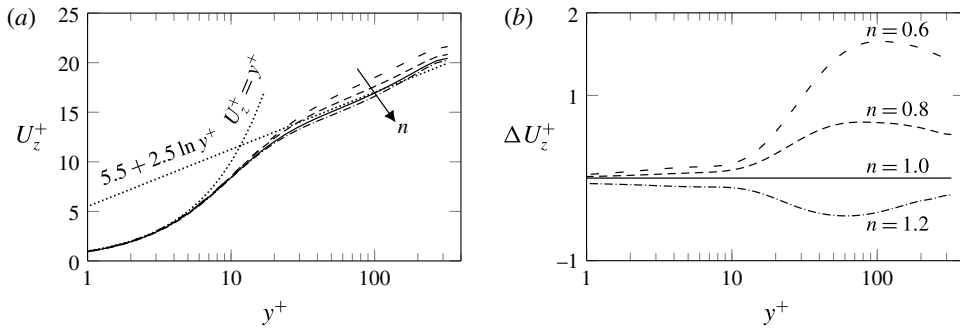FIGURE 7. (*a,b*) Streamwise integral length scales and (*c*) azimuthal integral length scale plotted as functions of y^+.

FIGURE 8. Profiles of (*a*) mean axial velocity U_z^+ and (*b*) difference between U_z^+ for a PL and Newtonian fluid plotted against y^+.

4. Mean flow and turbulence statistics

4.1. *Mean axial velocity and viscosity*

The effect of *n* is seen when the mean axial velocity, U_z^+, is plotted in wall coordinates (figure 8*a*), however, U_z^+ profiles show little variation when plotted in outer variables (not shown). For ease of discussion, the flow domain is nominally divided into four regions – the viscous sublayer ($y^+ < 5$), buffer layer ($5 < y^+ < 30$), log layer ($30 < y^+ < 200$) and core region ($y^+ > 200$). Although this flow domain subdivision is common for Newtonian fluids (Pope 2000), it will be seen that the delineation is not as obvious for GN fluids. In all subsequent discussion, when a trend is described as occurring with shear thinning ($n < 1$), it should be taken as read that the opposite trend occurs with shear thickening ($n > 1$).

In Newtonian fluids it is well known that the mean axial velocity profile in the viscous sublayer follows $U_z^+ = y^+$ which is the near-wall form of the law of the wall (Pope 2000). For PL fluids a similar viscous sublayer was anticipated in the analyses of Dodge & Metzner (1959) and Clapp (1961). For $n \neq 1$, a viscous sublayer appears in the mean axial velocity profiles (figure 8*a*), however, a close examination shows that the profiles for different *n* deviate slightly from the Newtonian case. This is more clearly seen in figure 8(*b*) where the difference (ΔU_z^+) between U_z^+ of the PL and Newtonian fluids is plotted against y^+. For all y^+, the U_z^+ profiles for shear-thinning GN fluids lie above the Newtonian profile (and *vice versa* for shear thickening).

Although the effect of flow index is seen at all y^+, ΔU_z^+ profiles deviate significantly from each other only beyond $y^+ \approx 10$. The maximum ΔU_z^+ occurs somewhere in the log layer with the exact location depending on the value of *n*. Note that the area integral of ΔU_z^+ at a cross-section represents the excess bulk flow rate and therefore, higher values of ΔU_z^+ indicate higher bulk flow (hence higher U_b) for lower *n* which was seen in table 1. Since τ_w is fixed in simulations, higher bulk velocity gives lower friction factor *f* for a more shear-thinning fluid. These results are consistent with those reported in previous studies (Dodge & Metzner 1959; Rudman *et al.* 2004; Rudman & Blackburn 2006). It is noted that the relative decrease in *f* compared to the Newtonian fluid (referred to as drag reduction, *DR*, in table 1) is approximately 14 % for $n = 0.6$ (see table 1), which is much less than that seen for viscoelastic fluids for which a drag reduction up to 70 % was observed in Ptasinski *et al.* (2001) at a comparable Reynolds number ($Re_G = 10\,000$).

Profiles of the normalised mean viscosity, $\nu^+ = \bar{\nu}/\nu_w$ ($\bar{\nu}$ is the time-averaged viscosity), show only minor dependence on *n* for $y^+ < 10$ with slightly higher values
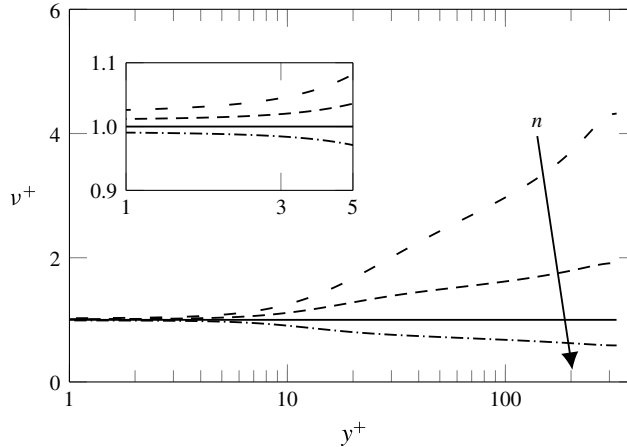
FIGURE 9. Profiles of the normalised mean viscosity $\nu^+ = \bar{\nu}/\nu_w$ plotted as a function of y^+. Detail in the viscous sublayer is shown in the inset figure.

for lower n (figure 9). At $y^+ = 10$, ν^+ is 1.25 (25 % higher than the nominal wall viscosity) for $n = 0.6$ and 1.10 for $n = 1.2$. Because viscosity of a shear-thinning fluid increases with decreasing shear rate, we expect the mean viscosity, ν^+, to increase monotonically towards the centre of the pipe for a shear-thinning fluid. For $n \neq 1$, mean viscosity profiles deviate rapidly from the wall value beyond $y^+ = 10$. The profiles of ν^+ appear to display a log-like region over the range $20 \lesssim y^+ \lesssim 200$, although the reasons for this are not yet understood.

4.2. *Mean shear stress budget*

Noting that the mean shear stress is zero at the pipe centre and τ_w at the wall, integration of (2.5) leads to the following expression for the (r, z) component of the mean non-dimensional shear stress:

$$\tau_{rz}^+ = \tau_{rz}^{\nu^+} + \tau_{rz}^{R^+} + \tau_{rz}^{f\nu^+} = \frac{r}{R} = \left(1 - \frac{y^+}{R^+}\right). \tag{4.1}$$

In a pipe flow, only the (r, z) component of the mean shear stress component remains, therefore subscript rz is dropped in the following discussion for clarity.

The effect of flow index n on the mean shear stress budget is shown in figure 10 where similar profiles of τ^{ν^+} and τ^{R^+} are seen for all n. As expected, the profile of the total mean shear stress is same for all n and is a straight line in linear coordinates with the maximum at the wall and zero at the pipe centre.

The mean viscous stress, τ^{ν^+}, is maximum at the wall and remains nearly constant until $y^+ \approx 3$ and then decreases towards the centre of the pipe. For shear-thinning fluids, τ^{ν^+} is higher than the Newtonian fluid across the entire radius. For the Newtonian fluid τ^{ν^+} drops to 5 % by $y^+ = 50$, however, for $n = 0.6$ it is still ≈ 15 % at $y^+ = 50$. It does not drop to 5 % until $y^+ \approx 200$, which indicates a significant thickening of the region over which the viscous stress plays a role as first suggested by Wilson & Thomas (1985). Note that $\tau^{\nu^+} = 2\nu^+ S_{rz}^+$, thus the increase in τ^{ν^+} with shear thinning could be a result of either increased ν^+ (see figure 9) or increased $S_{rz}^+ = (\partial U_z^+/\partial y^+)/2$ (see figure 11). From these figures, the increase in τ^{ν^+} in the
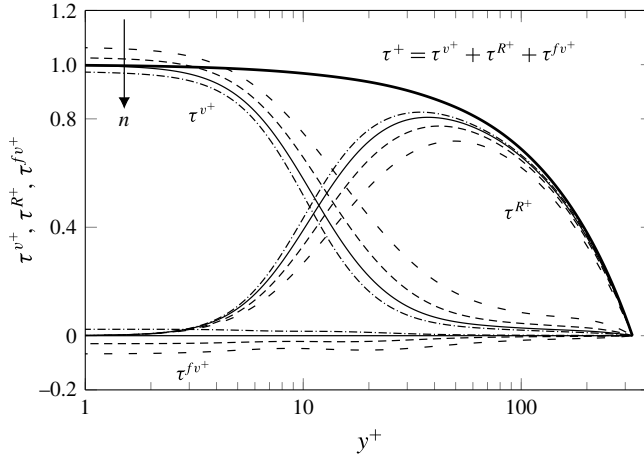
FIGURE 10. Profiles of the (r, z) component of the mean viscous stress, τ^{v^+}, Reynolds shear stress, τ^{R^+}, and the turbulent viscous stress, τ^{fv^+}, plotted for different n. The profile of the total mean stress τ^+ is linear and the same for all n and is given by (4.1).
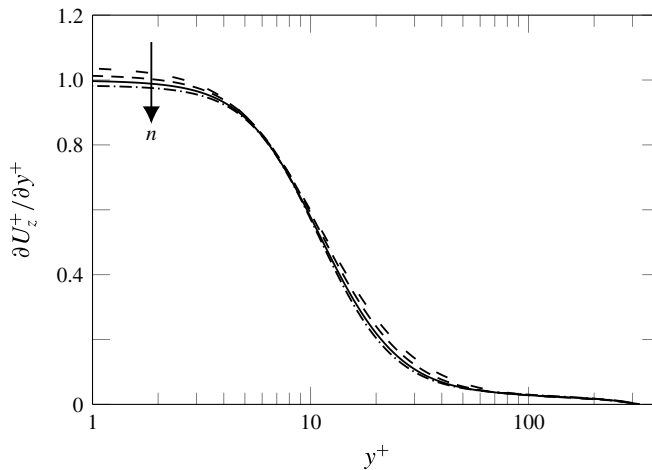

FIGURE 11. Profiles of the mean velocity gradient plotted as a function of y^+ for different n.

viscous sublayer is seen to be due to small increases in both ν^+ and S_{rz}^+. Beyond $y^+ > 10$, the increase in τ^{v^+} with shear thinning is primarily due to an increase in ν^+.

Outside the viscous sublayer, the increase in τ^{v^+} with shear thinning is compensated for primarily by a decrease in the Reynolds shear stress, τ^{R^+}. The maximum value of τ^{R^+} for the Newtonian fluid is approximately 80 % which occurs at $y^+ \approx 40$. In contrast, for $n = 0.6$, the maximum τ^{R^+} is approximately 70 % with the location of maximum τ^{R^+} moving away from the wall, $y^+ \approx 50$. These results are discussed further in § 4.5.

Since the Reynolds shear stress, τ^{R^+}, vanishes in the viscous sublayer, the increase here in mean viscous stress, τ^{v^+}, with shear thinning is compensated by a decrease in the turbulent viscous stress, τ^{fv^+}. Since $\tau^{fv^+} = 0$ for a Newtonian fluid, this results

in increasingly negative values of τ^{fv^+} for $n < 1$ as seen in figure 10. However, the contribution of τ^{fv^+} to the mean shear stress budget is small (approximately 5 % at the wall for $n = 0.6$). Note that we expect negative values of $\tau^{fv^+} = 2\overline{\nu' s'_{ij}}$ for a shear-thinning fluid because viscosity decreases with increase in shear rate.

Overall, the effect of increased shear thinning (decreasing n) on the mean shear stress budget is to increase the mean viscous stress and decrease the Reynolds shear stress. The turbulent viscous stress which is zero for a Newtonian fluid, becomes more negative with shear thinning, but is small compared to other components. It is noted that the turbulent viscous stress is determined here using the predicted viscosity and shear-rate fluctuations. It can also be determined as a deficit in the time-averaged shear stress as $\tau^{fv^+} = r/R - \tau^{v^+} - \tau^{R^+}$ (see (4.1)). This can be done from experimental measurements of the mean viscous stress and the Reynolds shear stress as done by Ptasinski *et al.* (2001, 2003) for viscoelastic fluids. Thus, a comparison of τ^{fv^+} between DNS and experiments is possible.

4.3. *Mean velocity gradient and wall units*

In the viscous sublayer, we observed a higher mean axial velocity at all y^+ for more shear-thinning fluids (see figure 8). This can be explained by considering (4.1) at the wall. Noting that $\tau^{v^+} = \nu^+(\partial U_z^+/\partial y^+)$ and τ^{R^+} and y^+/R^+ are zero at the wall, equation (4.1) can be used to write the mean axial velocity gradient at the wall as:

$$\frac{\partial U_z^+}{\partial y^+} \approx \frac{1}{\nu^+}(1 - \tau_{rz}^{fv^+}). \qquad (4.2)$$

For a Newtonian fluid $\tau^{fv^+} = 0$, and hence (4.2) gives $\partial U_z^+/\partial y^+ = 1$ which is the classical linear wall profile $U_z^+ = y^+$. However, τ^{fv^+} is negative for a shear-thinning fluid and its magnitude increases with shear thinning (figure 10). Although the mean viscosity at the wall, $\bar{\nu}_w$, increases slightly with shear thinning (figure 9), it does not compensate for the increase in τ^{fv^+} in (4.2). Thus higher $\partial U_z^+/\partial y^+$ with decreasing n results in a non-unitary slope of the mean axial velocity at the wall.

We fare no better if we replace the nominal wall viscosity, ν_w, used in the non-dimensionalisation by the mean wall viscosity $\bar{\nu}_w$ ($\bar{\nu}_w \neq \nu_w$). Doing this gives the distance from the wall in wall coordinates as $y^\ominus = yu^*/\bar{\nu}_w$ and allows (4.2) to be written as:

$$\frac{\partial U_z^+}{\partial y^\ominus} \approx (1 - \tau_{rz}^{fv^+}). \qquad (4.3)$$

Profiles of the mean axial velocity gradient for different n are shown in figure 12(*a*) using the above non-dimensionalisation. Because τ^{fv^+} is non-zero at the wall for shear-thinning fluids, it is clear from (4.3) that $\partial U_z^+/\partial y^\ominus \neq 1$, thus using $\bar{\nu}_w$ as the viscosity scale also does not provide the classical scaling. However, (4.3) suggests an alternative velocity scaling. Instead of using $\rho u^{*2} = \tau_w$, define a velocity scale via $\rho u^{\#2} = (\tau_w - \tau^{fv})$ and use $\bar{\nu}_w$ as the viscosity scale. This gives a non-dimensional distance from the wall $y^\oplus = yu^\#/\bar{\nu}_w$ and a non-dimensional velocity of $U_z^\oplus = U_z/u^\#$. Finally, it is straightforward to show that $\partial U_z^\oplus/\partial y^\oplus = 1$ and thus profiles of the mean axial velocity and its gradient collapse for different n in the viscous sublayer (figures 12*b* and 13).

A mitigating factor against using these new scales is that they are less practical. Neither $u^\#$ or $\bar{\nu}_w$ can be determined *a priori* in experiment or simulation. The mean
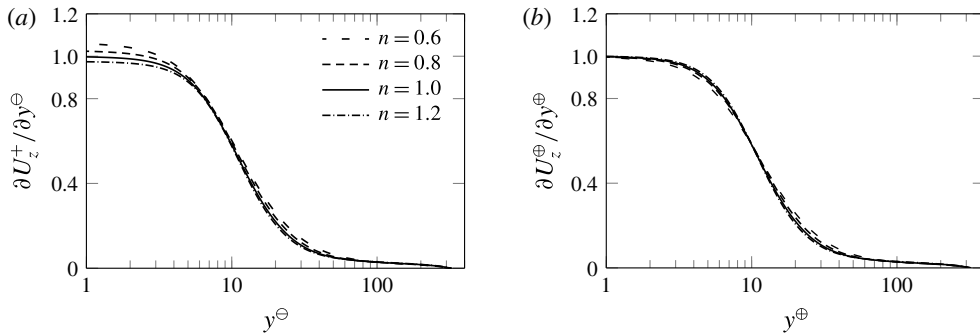
(a)

(b)

FIGURE 12. Profiles of the mean axial velocity gradient for different n where the non-dimensionalistion used (a) u^* for the velocity scale and the mean wall viscosity $\bar{\nu}_w$ for the viscosity scale, (b) $u^{\#}$ for the velocity scale and $\bar{\nu}_w$ for the viscosity scale.
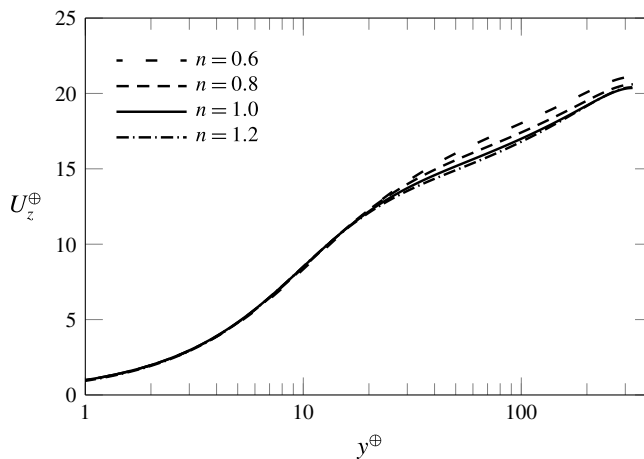

FIGURE 13. Mean axial velocity profiles plotted for different n using $u^{\#}$ for the velocity scale and $\bar{\nu}_w$ for the viscosity scale in non-dimensionalisation.

shear rate and axial velocity gradient required at the wall are difficult to measure accurately in experiment. Although the new scaling collapses near wall profiles of the mean axial velocity, its gradient and the mean viscous stress, profiles of other mean flow variables and correlations do not collapse for different n in the viscous sublayer (not shown). Finally, profiles of the total mean shear stress for different n no longer lie on top of each other because the shear stress scale $\rho u^{\#2}$ varies with n. Thus in the process of recovering one fundamental Newtonian relation, another fundamental relation is lost. As a consequence of these facts u^* and ν_w as mentioned in §2.3 are used in the non-dimensionalisation.

4.4. *Turbulence intensities*

The results presented in §4.1 show that the mean axial velocity, U_z^+, and the mean viscosity, ν^+, are only weakly dependent on n in the viscous sublayer. However, this is not the case for the axial turbulence intensity $u_z'^+$ as shown in figure 15(a). Here
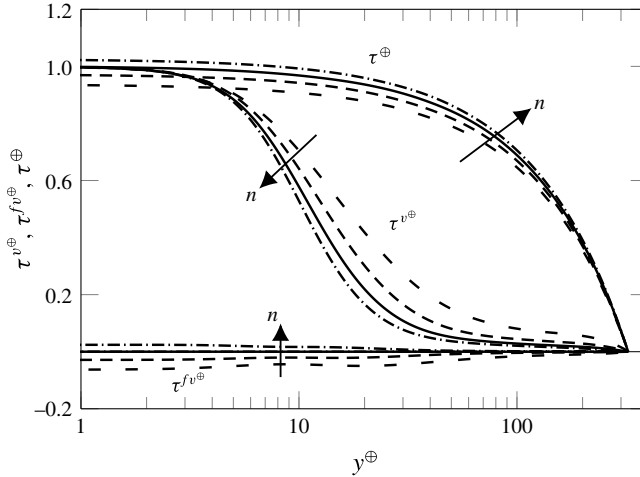
FIGURE 14. Profiles of the viscous stresses, τ^v and τ^{fv}, plotted for different n using $u^{\#}$ for the velocity scale and $(\bar{\nu})_w$ for the viscosity scale in non-dimensionalisation.

$u_z'^+$ increases with decreasing n at all y^+ and its peak moves further from the wall. For $n = 0.6$ the increase in the viscous sublayer is of order 25 %.

Unlike $u_z'^+$ which increased with shear thinning at all y^+, the radial and the azimuthal turbulence intensities ($u_r'^+$, $u_\theta'^+$) show dependence on n mainly outside the viscous sublayer, where they decrease with decreasing n (figure 15b,c). The location where profiles of $u_r'^+$, $u_\theta'^+$ for different n deviate significantly from each other coincides with the location where the mean viscosity ν^+ also deviates. This suggests that $u_r'^+$, $u_\theta'^+$ strongly depend on the mean fluid viscosity and that increased viscosity with decreasing n damps the velocity fluctuations normal to the mean flow direction. Note that the turbulence intensity profiles plotted in outer units (normalised by the bulk velocity U_b) also show similar trends (figure 15d–f). Both of these trends have been noted previously (Rudman *et al.* 2004; Rudman & Blackburn 2006; Gavrilov & Rudyak 2016) and have been suggested as being due to decreased energy transfer from axial velocity fluctuations to transverse velocity fluctuations via pressure fluctuations (Gavrilov & Rudyak 2016).

For a power-law fluid, root mean square (r.m.s.) viscosity fluctuations $\nu'^+ = \nu'_{rms}/\nu_w$ are non-zero at all y^+ and increase with shear thinning (figure 16a). Similar to the mean viscosity, ν'^+ remains uniform in the viscous sublayer and increases with y^+ outside the viscous sublayer, however, except for $n = 0.6$, the rate of increase in ν'^+ with y^+ is small. Profiles of ν'^+ normalised by the local mean viscosity show that ν'^+/ν^+ increases only up to a certain y^+, which increases with decreasing n, and then starts decreasing (figure 16b). Higher ν'^+ suggests higher instantaneous viscosities for a more shear-thinning fluid, which is also seen in figure 5.

4.5. *Quadrant analysis of Reynolds stresses*

We consider the quadrant analysis of Reynolds shear stress proposed by Wallace, Eckelmann & Brodkey (1972) and define $\tilde{v}_r' = -v_r'$ as the instantaneous wall-normal velocity fluctuations (v_r' has a different sign here because of the coordinate system employed). The analysis classifies the $v_z'\tilde{v}_r'$ signal into four different categories:
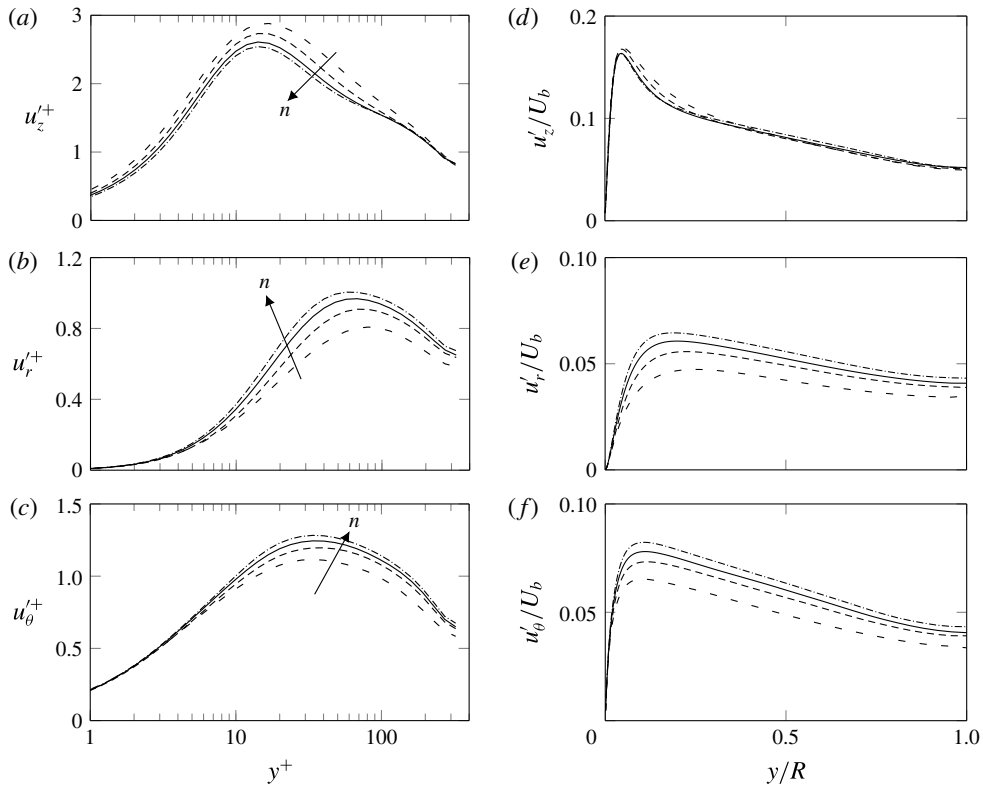
FIGURE 15. Profiles of turbulence intensities plotted in wall units (*a–c*) and in outer units (*d–f*) for different flow indices *n*.
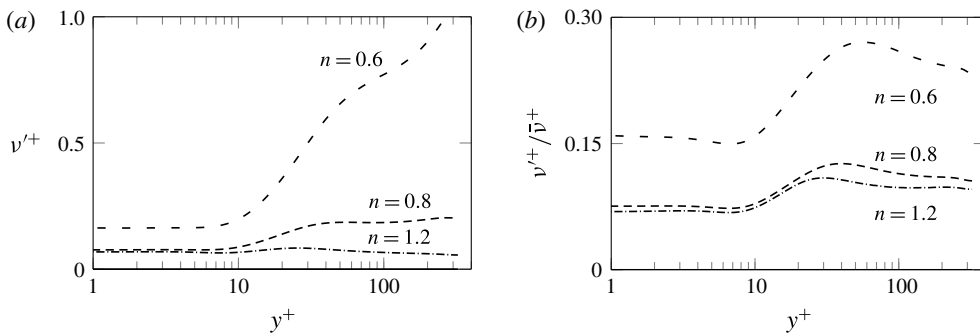

FIGURE 16. Profiles of root mean square viscosity fluctuations normalised by (*a*) the nominal wall viscosity ν_w and (*b*) mean viscosity, $\bar{\nu}(y^+)$ plotted for different *n*.

Q1($+v_z'$, $+\tilde{v}_r'$), Q2($-v_z'$, $+\tilde{v}_r'$), Q3($-v_z'$, $-\tilde{v}_r'$) and Q4($+v_z'$, $-\tilde{v}_r'$). These quadrants are associated with different physical events. For channel flows of Newtonian fluids, it has been found that most of the Reynolds shear stress production is associated with the ejection (Q2) and sweep (Q4) of low-speed fluid near the wall. Consequently they are also termed the ejection and sweep quadrants (see Wallace 2016).
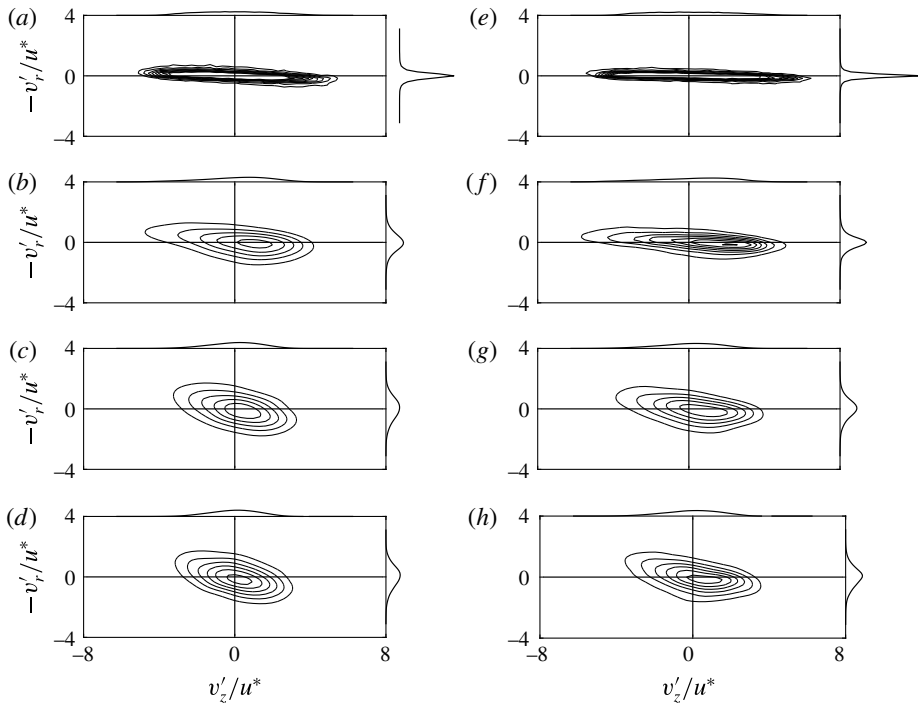
FIGURE 17. Joint and marginal probability distributions of the axial and wall-normal velocity fluctuations (v_z' and $-v_r'$) plotted at $y^+ = 10, 30, 70, 100$ (top to bottom) for (a–d) Newtonian and (e–h) $n = 0.6$.

Figure 17 compares the joint probability distribution $P(-v_r'/u^*, v_z'/u^*)$ of $n = 1.0$ and $n = 0.6$ for values of $y^+ = 10, 30, 70$ and 100. In the near-wall region, the major axis of $P(-v_r', v_z')$ is less inclined in the direction of Q2–Q4 for $n = 0.6$ (figure 17e–h) compared to the Newtonian fluid (figure 17a–d), which suggests that the shear-thinning rheology suppresses the contribution of ejection and sweep to Reynolds shear stress generation. Compared to the Newtonian fluid, a narrower spread of the marginal probability distribution $P(-v_r')$ for $n = 0.6$ in the near-wall region (seen clearly for $y^+ = 10$ and 30) suggests that with shear thinning, axial velocity fluctuations become larger than wall-normal fluctuations (as known from figure 15). Therefore, there is a less momentum exchange via the Reynolds shear stress in the wall-normal direction.

4.6. *Summary*

The key results in this section are that the effect of shear thinning is to increase the mean axial velocity, mean viscosity and axial turbulence intensity but, to decrease the radial and azimuthal turbulence intensities. The mean viscous stress increases slightly in the very-near-wall region and quite significantly in the buffer layer, and the distance from the wall where it drops to of order 5 % of the total stress is significantly increased. With shear thinning, the Reynolds shear stress decreases across the pipe and the new term in the mean shear stress balance, the turbulent viscous stress, is always negative, offsetting the increased mean viscous stress very

near the wall. This results in an increase in the mean axial velocity gradient and the bulk velocity (hence, the flow rate) with shear thinning.

5. Energy budgets

The total kinetic energy per unit mass is defined as $q = u_i u_i / 2$ and using the Reynolds decomposition, the mean kinetic energy is written as $\bar{q} = K + k$ where $K = U_i U_i / 2$ is the mean flow kinetic energy (MFKE) and $k = \overline{u_i' u_i'}/2$ is the turbulent kinetic energy (TKE). Non-uniform viscosity and viscosity fluctuations modify the MFKE and TKE budget equations for a non-Newtonian fluid. Since MFKE and TKE are scalar quantities, the choice of the coordinate system does not influence their budget equations and a Cartesian system is chosen here for clarity.

5.1. *Mean flow kinetic energy budget*

An equation for the MFKE can be obtained by taking the divergence of (2.5). In Cartesian coordinates this produces

$$
\overbrace{\frac{\partial K}{\partial t}}^{K_t} + \overbrace{U_j \frac{\partial K}{\partial x_j}}^{\mathcal{A}_m} = \overbrace{-U_j \frac{\partial P}{\partial x_j}}^{W_{dp/dz}} + \overbrace{\left(-\frac{\partial U_i \overline{u_i' u_j'}}{\partial x_j} \right)}^{\mathcal{T}^m} + \overbrace{2 \frac{\partial \bar{\nu} S_{ij} U_i}{\partial x_j}}^{\mathcal{D}^m} + \overbrace{(-2\bar{\nu} S_{ij} S_{ij})}^{\epsilon^m} + \overbrace{\overline{u_i' u_j'} S_{ij}}^{-\mathcal{P}}
$$

$$
+ \overbrace{2 \frac{\partial U_i \overline{v' s_{ij}'}}{\partial x_j}}^{\Upsilon_{nn}^m} + \overbrace{(-2\overline{v' s_{ij}' S_{ij}})}^{\chi_{nn}} . \tag{5.1}
$$

We use following terminology for different terms in (5.1):

K_t: local rate of change of K;
$\mathcal{A}^m$:   mean flow advection;
$W_{dp/dz}^+$: the mean flow energy production;
$\mathcal{T}^m$:   turbulent transport;
$\mathcal{D}^m$:   the mean viscous transport;
ϵ^m: the mean viscous dissipation;
$-\mathcal{P}$:   turbulent energy transfer or negative of turbulent kinetic energy production;
Υ_{nn}^m: the turbulent viscous stress transport;
χ_{nn}:   the mean shear turbulent viscous dissipation.

A subscript *nn* is used for terms which are non-zero only for a non-Newtonian fluid. The first two terms in (5.1) i.e. K_t and $\mathcal{A}^m$, are the rate of change and the mean advection of K both of which vanish for a pipe flow as the mean flow is temporally stationary, one component and uniform in the axial direction. The mean flow energy production, $W_{dp/dz}$, is the only source of energy in (5.1). The mean flow stresses common for both Newtonian and a non-Newtonian fluid ($\tau^v = 2\bar{\nu} S_{ij}$ and $\tau^R = -\overline{u_i' u_j'}$) appear at four places in (5.1) and play two roles; first, they redistribute the energy within the domain via the transport terms $\mathcal{D}^m$ and $\mathcal{T}^m$. Second, they act as a sink (ϵ^m and $-\mathcal{P}$). The transport terms cannot affect the global MFKE budget because the volume integral of each transport term is zero (Pope 2000). As we will see later, $-\mathcal{P}$ is the negative of the only source term in the TKE budget (see (5.2)) and therefore represents the energy transfer from the mean flow to the turbulence.
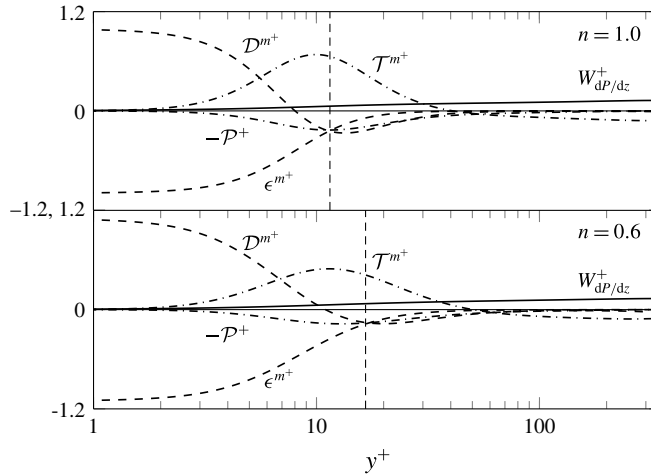
FIGURE 18. Profiles of the mean flow kinetic energy terms from (5.1) plotted in wall units for a Newtonian fluid (top) and $n = 0.6$ (bottom). Vertical lines show the location where $\mathcal{D}^{m^+}$, $-\mathcal{P}^+$ and ϵ^{m^+} intersect.

The last two terms in (5.1), Υ_{nn}^{m} and χ_{nn}, appear only for a non-Newtonian fluid. They arise from the interaction between the turbulent viscous stress, $\tau^{fv} = 2\overline{\nu' s_{ij}'}$, and the mean flow. The turbulent viscous transport, Υ_{nn}^{m}, is a transport term whereas the mean shear turbulent viscous dissipation, χ_{nn}, modifies the mean flow energy dissipation ϵ^{m}. This non-Newtonian dissipation term, χ_{nn}, also appears in the TKE budget (see (5.2)). Note that χ_{nn} can be positive or negative depending on the rheology of the fluid. However, positive values of χ_{nn} do not imply MFKE production. The mean flow can receive energy only through the action of pressure gradient against the mean flow and positive values of χ_{nn} instead correspond to a reduced mean flow kinetic energy dissipation.

To set the scene for subsequent discussion, we briefly describe the MFKE budget for a Newtonian fluid and plot the profiles of each term in figure 18. As the mean axial pressure gradient, $\mathrm{d}P/\mathrm{d}z$, is independent of r, profiles of the mean flow energy production, $W_{\mathrm{d}p/\mathrm{d}z}^{+}$, follow a similar trend as seen for U_z^{+} in figure 8(*a*) and $W_{\mathrm{d}p/\mathrm{d}z}^{+}$ increases with the distance from the wall. Very near the wall ($y^{+} < 3$), the MFKE budget is purely a balance between the two viscous terms, $\mathcal{D}^{m^+}$ and ϵ^{m^+}, because the Reynolds shear stress, τ^{R^+} vanishes here, as do the two terms that contain it (i.e. the Reynolds stress transport, $\mathcal{T}^{m^+}$, and the turbulent energy transfer, $-\mathcal{P}^+$).

Over the range $3 < y^{+} < 60$, there is a more complex balance between the Newtonian transport and dissipation terms, $\mathcal{T}^{m^+}$, $\mathcal{D}^{m^+}$, ϵ^{m^+} and $-\mathcal{P}^+$. For $y^{+} > 3$, both $\mathcal{T}^{m^+}$ and $-\mathcal{P}^+$ grow in magnitude with $\mathcal{T}^{m^+}$ adding energy in this region and $-\mathcal{P}^+$ dissipating it , with both terms reaching their maximum effect at $y^{+} \approx 10$. The mean viscous transport, $\mathcal{D}^{m^+}$, is a sink for $y^{+} > 8$ and source for $y^{+} < 8$, which means that it transports energy to the viscous sublayer because its volume integral is zero. The turbulent kinetic energy production, $-\mathcal{P}^+$, is significant only for $3 \lesssim y^{+} \lesssim 40$ and it reaches a maximum approximately at the same location where $\mathcal{D}^{m^+}$ and ϵ^{m^+} cross each other as also noted in Thais, Gatski & Mompean (2013) for viscoelastic fluids.

The Reynolds shear stress transport, $\mathcal{T}^{m^+}$, continues acting as a source up to $y^{+} \approx 40$ where it changes sign due to the change in the slope of the Reynolds shear stress (see
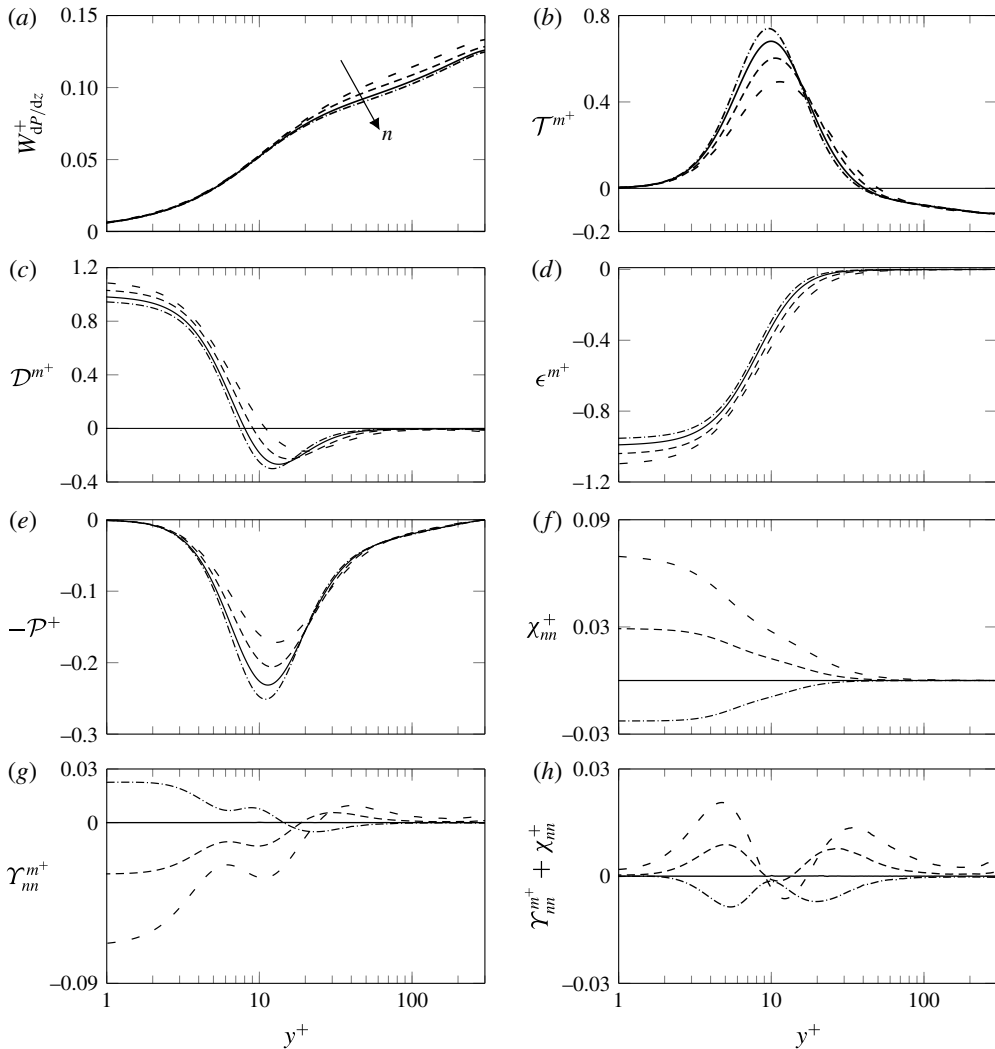
FIGURE 19. Profiles of the mean flow kinetic energy budget terms from (5.1) plotted for different flow indices n in wall variables. Note that the vertical scale changes in each plot.

figure 10). It then acts as a sink and therefore, transports energy from $y^+ > 40$ towards the wall. For $y^+ > 60$, the MFKE budget is mainly a balance between $\mathcal{T}^{m^+}$ and $W_{dP/dz}^+$ because the turbulent kinetic energy production, $-\mathcal{P}^+$, is very small and approaches zero at the pipe centre.

The effect of changes in flow index on individual mean flow energy budget terms is shown in figures 18 and 19. We first discuss the effect of shear thinning on those terms that also appear for a Newtonian fluid before examining the modifications resulting to the non-Newtonian terms. As mentioned earlier also, when a trend is described as occurring with shear thinning, it should be taken as read that the opposite trend occurs with shear thickening.

As already noted in §4.1, the mean axial velocity profile for a shear-thinning fluid lies above the Newtonian profile and consequently the mean flow energy production,

$W_{\mathrm{d}P/\mathrm{d}z}^{+}$, must increase with shear thinning as seen in figure 19(*a*). However, with the exception of $W_{\mathrm{d}P/\mathrm{d}z}^{+}$, most terms show little variation with *n* beyond $y^{+} \approx 60$ although there are sufficient differences to balance the increased production, these are not obvious given the required figures axis scaling. The radial location where the two viscous terms, $\mathcal{D}^{m^{+}}$ and $\epsilon^{m^{+}}$, intersect each other is also shifted by shear thinning as seen in figure 18.

The mean axial velocity gradient, $\partial U_{z}^{+}/\partial y^{+}$, and hence the mean viscous stress, $\tau^{v^{+}}$, increases with decreasing *n* (figure 10), therefore, more negative $\epsilon_{m}^{v^{+}}$ is observed with decreasing *n* in figure 19(*d*). Since the gradient of $\tau^{v^{+}}$ is also less negative for a more shear-thinning fluid further from the wall, higher values of $\mathcal{D}^{m^{+}}$ result until $y^{+} \approx 15$–20 where this term becomes slightly less negative for a more shear-thinning fluid (figure 19*c*). Similarly, lower Reynolds stress with decreasing *n* (figure 10) results in less negative turbulent energy transfer, $-\mathcal{P}^{+}$, (figure 19*e*) and lower values of the Reynolds stress transport, $\mathcal{T}^{m^{+}}$, up to approx $y^{+} \approx 20$ at which point the latter term becomes a little higher with shear thinning (figure 19*b*). As discussed later in §5.2, $-\mathcal{P}^{+}$ appears with opposite sign in the turbulent kinetic energy budget as a production term. Thus the decrease in magnitude of $-\mathcal{P}^{+}$ observed here with shear thinning means there is a less energy transferred via this mechanism into turbulence. The combination of higher MFKE production, $W_{\mathrm{d}P/\mathrm{d}z}^{+}$, and less energy transfer to turbulence via $-\mathcal{P}^{+}$ suggests that there will be higher dissipation by the mean viscous stress ($\epsilon^{m^{+}}$) in case of lower *n* – this may be observed in figure 19(*d*).

The two non-Newtonian terms, $\Upsilon_{nn}^{m^{+}}$ and χ_{nn}^{+}, vary most significantly for $y^{+} < 60$, similarly to the Newtonian transport and dissipation terms. However, their magnitude is approximately one order less than the $\mathcal{D}^{m^{+}}$ and $\epsilon^{m^{+}}$ and they play a smaller role in the MFKE balance. The non-Newtonian dissipation, χ_{nn}^{+}, is negatively related to $\tau^{fv^{+}}$ which was seen to be negative for a shear-thinning fluid (figure 10). Thus we expect χ_{nn}^{+} to be positive for shear-thinning fluids (as seen in figure 19*f*) and this reduces dissipation. However, the sum of $\epsilon^{m^{+}}$ and χ_{nn}^{+} (figure 20*a*) shows that the net effect of these two viscous dissipation terms only slightly increases the magnitude of dissipation in the very near wall and buffer layer. The non-Newtonian transport term, $\Upsilon_{nn}^{m^{+}}$, changes sign in $y^{+} \approx 15$–20 (depending on *n*) and for shear thinning acts as a sink of the mean flow energy for $y^{+} \lesssim 15$ and a source further away from the wall. Overall, except in a narrow region near $y^{+} \approx 10$, the non-Newtonian terms act as a source for shear-thinning fluids and as a sink for the shear-thickening fluid ($n = 1.2$) in the MFKE budget at all y^{+} (figure 19*h*).

In summary, the mean flow energy production increases with shear thinning outside the buffer layer. For all other terms, the overall effect of decreasing flow index is to modify the MFKE budget terms most significantly in the near-wall region $y^{+} \lesssim 60$. The total viscous dissipation increases with shear thinning but the turbulent energy transfer (which peaks at $y^{+} \approx 10$) becomes less negative. The magnitude of the total viscous transport is also increased with shear thinning. The turbulent transport which is the mean flow energy transfer via the Reynolds shear stress which peaks at $y^{+} \approx 10$ and decreases with shear thinning. The non-Newtonian terms largely act as a source in the MFKE budget for shear-thinning fluids. In the total transport and dissipation profiles the shear-thinning effect almost disappears in $4 \lesssim y^{+} \lesssim 10$ (figure 20*b*).
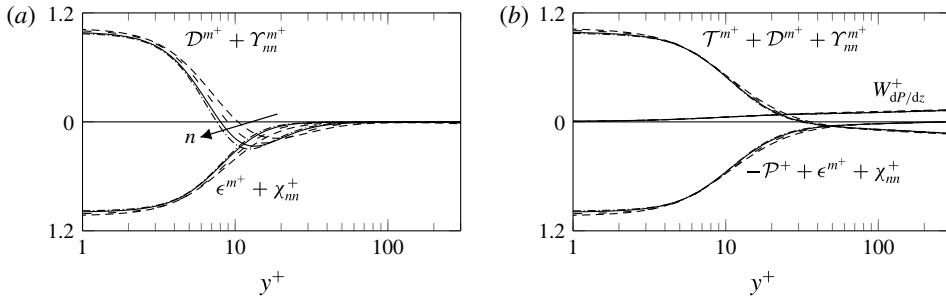
FIGURE 20. Profiles of the sum of Newtonian and non-Newtonian (*a*) viscous transport and dissipation terms (*b*) total transport and dissipation in (5.1) plotted for different flow indices *n*.

5.2. *Turbulent kinetic energy budget*

The equation for the ensemble-average turbulent kinetic energy ($k = \overline{u_i' u_i'}/2$) is

$$
\overbrace{\frac{\partial k}{\partial t}}^{k_t} + \overbrace{U_j \frac{\partial k}{\partial x_j}}^{\mathcal{A}} = \overbrace{-\overline{u_i' u_j'} S_{ij}}^{\mathcal{P}} + \left\{ \overbrace{-\frac{1}{2} \frac{\partial \overline{u_i' u_i' u_j'}}{\partial x_j}}^{\mathcal{T}} \overbrace{- \frac{\partial \overline{p' u_j'}}{\partial x_j}}^{\Pi} \overbrace{+ \frac{\partial (2\bar{\nu} \overline{s_{ij}' u_i'})}{\partial x_j}}^{\mathcal{D}} \right\} \overbrace{- 2\bar{\nu} \overline{s_{ij}' s_{ij}'}}^{\epsilon}
$$

$$
+ \left\{ \overbrace{\frac{\partial (\overline{2\nu' u_i' S_{ij}})}{\partial x_j}}^{\xi_{nn}} + \overbrace{\frac{\partial (\overline{2\nu' s_{ij}' u_i'})}{\partial x_j}}^{\mathcal{D}_{nn}} \right\} \overbrace{- 2\overline{\nu' s_{ij}'} S_{ij}}^{\chi_{nn}} \overbrace{- 2\overline{\nu' s_{ij}' s_{ij}'}}^{\epsilon_{nn}} . \tag{5.2}
$$

Here, the terms in the first row appear for both Newtonian and non-Newtonian fluids and the following is the standard terminology:

k_t: rate of change of turbulence kinetic energy;
$\mathcal{A}$:   mean flow advection;
$\mathcal{P}$:   turbulent kinetic energy production;
$\mathcal{T}$:   turbulent velocity transport;
Π: pressure related transport;
$\mathcal{D}$:   mean viscous transport;
ϵ: mean viscous dissipation.

The remaining terms i.e. the terms in the second row in (5.2) are zero for a Newtonian fluid and appear only for a fluid with non-uniform viscosity. We adopt the following terminology for these terms:

ξ_{nn}:   mean shear turbulent viscous transport;
$\mathcal{D}_{nn}$:   turbulent viscous transport;
χ_{nn}:   mean shear turbulent viscous dissipation;
ϵ_{nn}:   turbulent viscous dissipation.

When the terms of similar nature are summed together TKE budget equation can be written as:

$$\frac{\mathrm{D}k}{\mathrm{D}t} = \mathcal{P} + T^k - \epsilon^k. \tag{5.3}$$

Here, $T^k = \mathcal{T} + \Pi + \mathcal{D} + \mathcal{D}_{nn} + \xi_{nn}$ is the total transport and $\epsilon^k = \epsilon + \chi_{nn} + \epsilon_{nn}$ is the total dissipation. As with the MFKE budget (5.1), the first two terms in (5.2), k_t and $\mathcal{A}$ vanish for a pipe flow and the local TKE budget is maintained by a balance between the remaining terms. As already mentioned in §5.1, the turbulent kinetic energy production $\mathcal{P}$, is the only source term in (5.2) and it couples the MFKE and the TKE budget equations. The mean viscous dissipation, ϵ, is negative definite and as the name says, is the dissipation of TKE due to the mean viscosity. The gradient terms, $\mathcal{T}$, Π, $\mathcal{D}$, only redistribute TKE, k, within the domain. Although they cannot produce or dissipate TKE, they can be local sources or sinks in (5.2).

Remaining terms, ξ_{nn}, $\mathcal{D}_{nn}$, χ_{nn} and ϵ_{nn} are zero for a Newtonian fluid as they depend on viscosity fluctuations. We refer these as non-Newtonian TKE budget terms. The gradient terms, the mean shear turbulent viscous transport, ξ_{nn}, and the turbulent viscous transport, $\mathcal{D}_{nn}$ either enhance or diminish the transport by the Newtonian transport terms. The mean shear turbulent viscous dissipation, χ_{nn} appears in both the MFKE and the TKE budgets with the same sign, meaning that it affects both energy budgets in a similar manner. Both χ_{nn} and ϵ_{nn} appear as source/sink terms in TKE budget, although neither is obviously positive (or negative) definite for shear-thinning fluids. As mentioned in §5.1 for χ_{nn}, positive values of either of these terms does not mean that they are true sources of turbulent energy. Turbulence can only source energy from the mean flow and although χ_{nn} involves the mean flow via S_{ij}, its genesis is in the total viscous dissipation and as such it is clearly part of the total turbulent dissipation. The turbulent viscous dissipation, ϵ_{nn}, has a similar genesis and is more clearly associated with dissipation.

The effect of flow index n on the individual terms in (5.2) is shown in figure 21. Turbulence kinetic energy production, $\mathcal{P}^+$, decreases with shear thinning over $3 < y^+ < 20$ with the peak shifting slightly away from the wall (figure 21a). Production is the product $-\overline{u_i' u_j'} S_{ij}$ and for a pipe flow, only the S_{rz} component survives, which gives $\mathcal{P}^+ = \tau^{R^+}(\partial U_z^+/\partial y^+)/2$. Since S_{rz}^+ is little affected by shear thinning for $3 < y^+ < 20$ (figure 11), the observed decrease in $\mathcal{P}^+$ with shear thinning is primarily due to the decrease in Reynolds shear stress (figure 10).

As n decreases, turbulent kinetic energy dissipation, $\epsilon^+ = 2\nu^+ \overline{s_{ij}' s_{ij}'}^+$, increases in magnitude for all y^+, although most noticeably for $y^+ < 5$ and then less so over $20 < y^+ < 100$ (figure 21a). The increased dissipation over $20 < y^+ < 100$ is due to the increase in mean viscosity with shear thinning (figure 9) since $\overline{s_{ij}' s_{ij}'}^+$ decreases here for all n (figure 22a). However, the increase in ϵ^+ with decreasing n close to the wall is due to increased strain-rate fluctuations $\overline{s_{ij}' s_{ij}'}$ with decreasing n as the mean viscosity is only weakly dependant on n (figure 9).

Profiles of the three Newtonian transport terms, $\mathcal{D}^+$, $\mathcal{T}^+$ and Π^+, are shown in figure 21(a–c). The mean viscous transport, $\mathcal{D}^+$, is the largest in magnitude and shows flow index dependence mostly in the viscous sublayer where it increases with shear thinning (figure 21a), partly countering the more negative dissipation for lower n. Recalling that (i) $\mathcal{D}^+$ is the gradient of $2\nu^+ \overline{s_{ij}'^+ u_i'^+}$ (see (5.2)), (ii) that only the radial derivative survives and (iii) that the mean viscosity, ν^+, is almost constant in
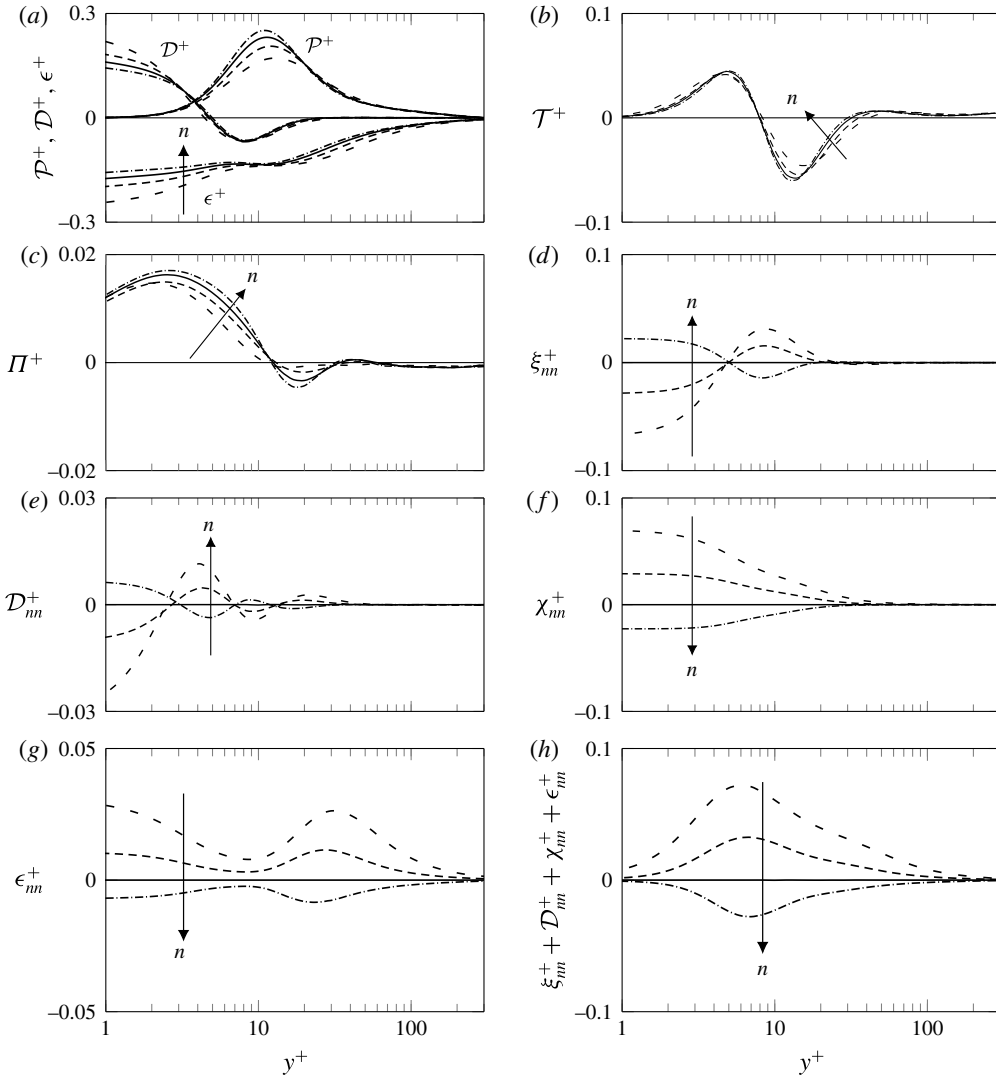
FIGURE 21. Profiles of the turbulent kinetic energy budget terms (see (5.2)) plotted for different flow indices n in wall variables. Note that the vertical scale changes in each plot.

the viscous sublayer (figure 9), we draw the conclusion that larger $\mathcal{D}^+$ for lower n is due to more rapid increase in $\overline{s'_{ri}u'_i}^+$ in the viscous sublayer with shear thinning.

The main effect of decreasing n on the turbulent velocity transport, $\mathcal{T}^+$, is flattening and broadening of the profile in $8 < y^+ < 50$ (figure 21b). The contribution of the pressure related transport, Π^+, is small compared to the other transport terms (figure 21c) and although its magnitude is reduced in the viscous sublayer and buffer layer with shear thinning, this has a little effect on the total turbulent energy transport.

Overall, the effect of reducing flow index on the Newtonian terms in TKE budget is to elevate the mean viscous transport, $\mathcal{D}^+$ and turbulent dissipation, ϵ^+, close to the wall ($y^+ < 3$), and to decrease turbulent kinetic energy production, $\mathcal{P}^+$, near $y^+ = 10$.
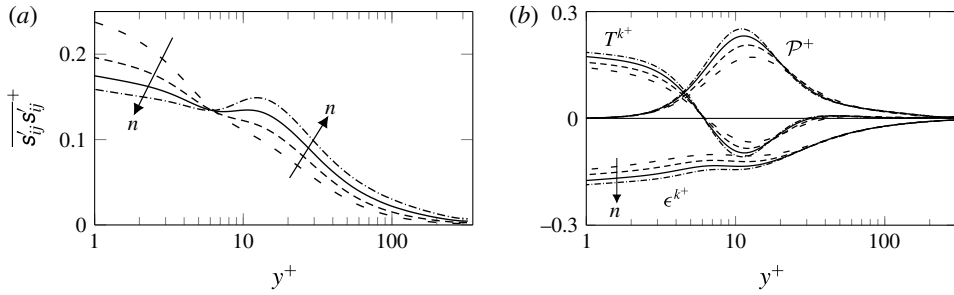
FIGURE 22. Profiles of (*a*) $\overline{s'_{ij}s'_{ij}}^+$ (*b*) turbulent kinetic energy production ($\mathcal{P}^+$), total dissipation ($\epsilon^{k^+} = \epsilon^+ + \chi_{nn}^+ + \epsilon_{nn}^+$) and transport ($T^{k^+} = \mathcal{T}^+ + \Pi^+ + \mathcal{D}^+ + \mathcal{D}_{nn}^+ + \xi_{nn}^+$) plotted in wall units.

The non-Newtonian transport terms, the mean shear turbulent viscous transport, ξ_{nn}^+, and the turbulent viscous transport, $\mathcal{D}_{nn}^+$, are significant only for $y^+ \lesssim 40$ and the magnitude of both increases with shear thinning (figure 21*d,e*). The contribution of ξ_{nn}^+ to the turbulent kinetic energy budget at the wall is significant. It is approximately 25 % of the total Newtonian transport ($\mathcal{T}^+ + \Pi^+ + \mathcal{D}^+$) for $n = 0.6$ and approximately 13 % for $n = 0.8$ there. For $y^+ < 5$, ξ_{nn}^+ acts opposite to the Newtonian viscous transport, $\mathcal{D}^+$. At $y^+ \approx 5$, ξ_{nn}^+ changes sign (as does $\mathcal{D}^+$) and continues to act in an opposite sense to $\mathcal{D}^+$ for $5 \lesssim y^+ \lesssim 30$. This opposition is expected from the opposite signs of the mean viscous stress, τ^{v^+}, and the turbulent viscous stress, τ^{fv^+} (see figure 10). The contribution of $\mathcal{D}_{nn}^+$ to the turbulent kinetic energy budget is small (< 10 % of the Newtonian transport for $n = 0.8$). It changes sign several times and acts both against and with $\mathcal{D}^+$ over different regions of y^+. The sum of all transport terms ($\mathcal{T}^+ + \Pi^+ + \mathcal{D}^+ + \mathcal{D}_{nn}^+ + \xi_{nn}^+$) is shown in figure 22*b* where it is seen that the effect of shear thinning is to reduce the transport by the Newtonian terms for $y^+ \lesssim 20$ and to increase it marginally over $20 \lesssim y^+ \lesssim 70$.

The other two non-Newtonian terms, the mean shear turbulent viscous dissipation, χ_{nn}^+, and the turbulent viscous dissipation, ϵ_{nn}^+, are positive for shear-thinning fluids and negative for shear thickening (figure 21*f,g*). As previously mentioned, they are identified as dissipation terms that act to reduce the mean flow dissipation ϵ^+ over the entire pipe radius, but particularly for $y^+ < 40$. For $n = 0.6$ they reduce the dissipation in the viscous sublayer close to the wall by approximately 40 %. Their net effect is most clearly seen in figure 22(*a*) where the total dissipation is seen to reduce with shear thinning for $y^+ \lesssim 30$ with the reduction balancing the reduction in net transport for $y^+ < 5$ and partially balancing the reduction in production observed around $y^+ \approx 10$.

In the very near-wall region, ξ_{nn}^+ and χ_{nn}^+ almost cancel each other, as do $\mathcal{D}_{nn}^+$ and ϵ_{nn}^+, resulting in no net effect of the non-Newtonian TKE budget terms at the wall. The net effect of these terms increases through the viscous sublayer reaching a maximum near $y^+ \approx 7$ before slowly decreasing again out to $y^+ \gtrsim 100$ (figure 21*h*). They thus provide an additional source of energy in the TKE budget for shear-thinning fluids.

A summary of the effects of flow index modification is shown in figure 22(*b*) where the turbulent kinetic energy production, total transport and dissipation are compared for different *n*. They show flow index dependence only for $y^+ \lesssim 70$ and shear thinning is seen to reduce the magnitude of each, albeit over different ranges of y^+.
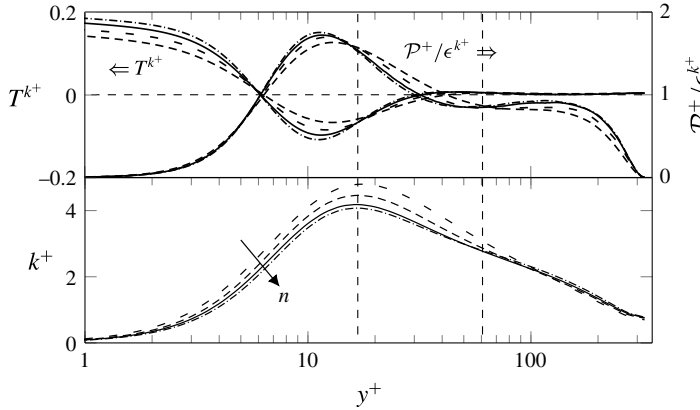
FIGURE 23. Profiles of the ratio of turbulent kinetic energy production to total dissipation ($\mathcal{P}^+/\epsilon^{k^+}$), total transport ($T^{k^+}$) and the turbulent kinetic energy k^+ plotted in wall units.
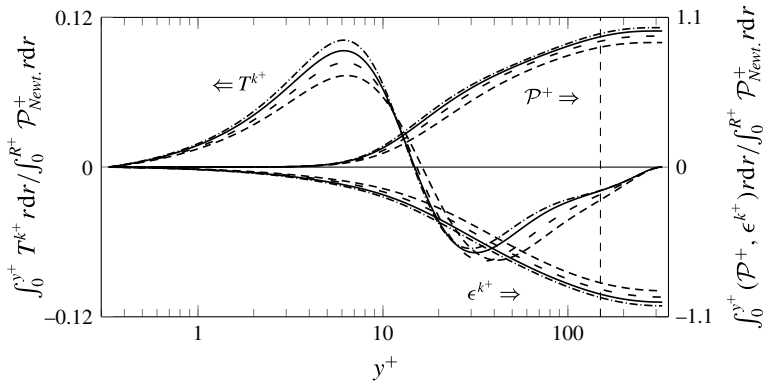

FIGURE 24. Integrated budget of turbulent kinetic energy production ($\mathcal{P}^+$), transport ($\mathcal{T}^+ + \Pi^+ + \mathcal{D}^+ + \mathcal{D}^+_{nn} + \xi^+_{nn}$) and dissipation ($\epsilon^+ + \chi^+_{nn} + \epsilon^+_{nn}$), normalised by the total Newtonian turbulent kinetic energy production (volume integral of $\mathcal{P}^+$ for $n = 1$) plotted for different n. The primary axis on the left is for the turbulent transport budget and the secondary axis on the right is for the turbulent kinetic energy production and dissipation.

Shear thinning widens the production region (where production exceeds the total dissipation) by increasing its upper bound (figure 23) whereas the lower bound remains fixed at $y^+ \approx 6$. In this region, the total transport becomes negative and thus carries the excess energy ($\mathcal{P}^+ - \epsilon^{k^+}$) away from the production region. The ratio of production to total dissipation ($\mathcal{P}^+/\epsilon^{k^+}$) is increased for $15 \lesssim y^+ \lesssim 60$ but decreased for $6 \lesssim y^+ \lesssim 15$ and beyond $y^+ \approx 60$ with shear thinning.

Profiles of the turbulent production, total dissipation and transport when integrated over the pipe cross-section show that shear thinning globally decreases the overall turbulent kinetic energy production and hence the total dissipation (figure 24). Beyond $y^+ = 150$, profiles of the integrated production and total dissipation for all n are almost flat showing that most of the turbulent production and dissipation occurs for $y^+ \gtrsim 150$. Profiles of the integrated total turbulent transport (which also represents negative of the extra energy available for turbulence i.e. $-(\mathcal{P}^+ - \epsilon^{k^+})$) show that there is more energy available (T^{k^+} is more negative for $y^+ \gtrsim 25$) for turbulence for

a more shear-thinning fluid. This suggests that shear thinning decreases dissipation more than it decreases the production.

Using the results of $\mathcal{P}^+/\epsilon^{k^+}$ shown in figure 23, the turbulent kinetic energy profiles for different n can be explained. The turbulent kinetic energy k^+ peaks at $y^+ \approx 15$ which is slightly higher than the location where $\mathcal{P}^+/\epsilon^{k^+}$ attains a maximum and approximately the same location where $\mathcal{P}^+/\epsilon^{k^+}$ profiles for different n cross each other. Over the region $15 \lesssim y^+ \lesssim 60$, higher production than dissipation results in higher k^+ for more shear-thinning fluids. A part of this higher k^+ is transported away from the wall and part towards the wall. For $y^+ > 60$, there is more dissipation for a lower n which dissipates the extra energy available for a more shear-thinning fluid and the k^+ profiles of different n collapse on top of each other for $y^+ \gtrsim 90$. For $y^+ < 15$, there is a narrow region ($y^+ = 6 - 15$) where $\mathcal{P}^+/\epsilon^{k^+}$ is clearly lower for a more shear-thinning fluid and therefore, the turbulent kinetic energy profiles slowly converge to a single curve towards the wall.

5.3. *Summary of results of energy budgets*

Results of the MFKE budget show that except the MFKE production, all other terms show flow index dependence only near the wall for $y^+ \lesssim 60$. Shear thinning increases the MFKE production and hence dissipation. The non-Newtonian terms are a source in the MFKE budget for a shear-thinning fluid and sink for the shear thickening. Similar to the MFKE budget terms, TKE budget terms are also dependent on n only near the wall. Shear thinning decreases the turbulent kinetic energy production in the buffer layer whereas it increases the turbulent transport and the mean viscous dissipation primarily in the viscous sublayer. The non-Newtonian terms act as a source in the TKE budget. The non-Newtonian dissipation terms in both MFKE and TKE are positive for a shear-thinning fluid and therefore decrease the total viscous dissipation.

6. Conclusions

The present study investigates the effect of the flow index parameter n on the turbulent pipe flow at a friction Reynolds number of 323. DNS results of the mean flow and turbulent kinetic energy budgets are presented for turbulent pipe flow of a GN fluid for the first time. Qualitative features of the flow for different n exhibits quite different flow structures and the range of flow length scales increases with increasing n. When the results are scaled with the nominal wall viscosity ν_w and the traditional friction velocity u^*, the mean axial velocity profiles of a power-law fluid do not strictly follow $U_z^+ = y^+$ in the viscous sublayer and the mean axial velocity gradient increases as n is decreased. New velocity and viscosity scales are derived, which collapse the mean axial velocity profiles in the viscous sublayer for different n. However, these new scales are difficult to determine in experiments and result in the total non-dimensional stress profiles no longer lying on top of each other for different n. Mean axial velocity profiles for different n show large deviation in the log layer and lie above the Newtonian profile for shear-thinning fluids. The mean viscosity increases with decreasing n however, the effect is seen clearly only outside the viscous sublayer. The cause of a log-like region seen in the mean viscosity profiles remains unknown. Turbulence intensities when expressed in wall units are found to increase in the axial direction but decrease in the radial and the azimuthal direction with decreasing n. This is likely due to the decrease in the turbulent energy transfer from the axial component to others as suggested by Gavrilov & Rudyak (2016).

The Reynolds shear stress is also found to decrease with decreasing n. Due to viscosity fluctuations a new term is introduced in the mean momentum balance: the turbulent viscous stress which is negative for a shear-thinning fluid and positive for the shear-thickening fluid. The magnitude of the turbulent viscous stress is maximum at the wall, however, there is no obvious reason why this should be the case. For unreported results of other rheologies, we observed it to be maximum away from the wall. Due to increased viscosity and mean shear rate, the mean viscous stress increase with decreasing n and the range of y^+ where its effect can be ignored increases with decreasing n, which suggests the thickening of the viscous sublayer by shear thinning.

Except for the mean flow energy production, the effect of n is seen on the mean flow energy budgets mostly for $y^+ < 60$. The mean flow energy production and dissipation increase with decreasing n and the non-Newtonian terms act as a source in the mean flow kinetic energy budget for shear-thinning fluids. Similar to the mean flow kinetic energy, the turbulent kinetic energy budget terms also show flow index dependence largely for $y^+ < 60$. The flow index n has a notable effect on turbulent kinetic energy production in the buffer layer, whereas it affects the mean viscous dissipation and turbulent transport largely in the viscous sublayer. The new terms introduced in the turbulent kinetic energy budget from the non-Newtonian rheology are found to add a source for a shear-thinning fluid and sink for a shear-thickening fluid. The current results for shear-thinning fluids are qualitatively similar to those for viscoelastic fluids, however, further investigation is required for the quantitative comparison between these two types of fluids.

In the current simulations, the mean axial velocity profiles shift away from the Newtonian profile with shear thinning. This kind of shift has been observed even for Newtonian fluids at lower Reynolds number. Contours of the instantaneous axial velocity showed less developed turbulence in the flow for lower n. Therefore, the question remains whether the observed shifting of the mean axial velocity profiles in current simulations is a Reynolds number effect or a rheology effect. Simulations at higher Reynolds numbers will answer this question. High Reynolds number simulations are also needed to show if log layer in the mean viscosity profiles is real or not. The current simulations have shown that the turbulent kinetic energy budget is affected by shear thinning only in the near-wall region ($y^+ < 60$). A question arises as to whether generalised Newtonian rheology is important only in $y^+ < 60$ and the deviation in the mean axial velocity and turbulence intensity profiles with shear thinning in the log layer is due to only to what happens close to the wall. This is the focus of ongoing research.

Acknowledgements

REFERENCES

BLACKBURN, H. M. & SHERWIN, S. J. 2004 Formulation of a Galerkin spectral element–Fourier method for three-dimensional incompressible flows in cylindrical geometries. *J. Comput. Phys.* **197** (2), 759–778.

CHHABRA, R. P. & RICHARDSON, J. F. 2008 *Non-Newtonian Flow and Applied Rheology*, 2nd edn. Elsevier.

CHILTON, R. & STAINSBY, R. 1998 Pressure loss equations for laminar and turbulent non-Newtonian pipe flow. *J. Hydraul. Engng ASCE* **124** (5), 522–529.

CHIN, C., MONTY, J. P. & OOI, A. 2014 Reynolds number effects in dns of pipe flow and comparison with channels and boundary layers. *Intl J. Heat Fluid Flow* **45**, 33–40.

CHIN, C., OOI, A. S. H., MARUSIC, I. & BLACKBURN, H. M. 2010 The influence of pipe length on turbulence statistics computed from direct numerical simulation data. *Phys. Fluids* **22** (11), 115107.

CLAPP, R. M. 1961 Turbulent heat transfer in pseudoplastic non-Newtonian fluids. *Intl Developments in Heat Transfer, ASME, Part III, Sec. A* 652–661.

CRUZ, D. O. A. & PINHO, F. T. 2003 Turbulent pipe flow predictions with a low Reynolds number $k - \varepsilon$ model for drag reducing fluids. *J. Non-Newtonian Fluid Mech.* **114** (2), 109–148.

DODGE, D. W. & METZNER, A. B. 1959 Turbulent flow of non-Newtonian systems. *AIChE J.* **5**, 189–204.

EGGELS, J. G., UNGER, F., WIESS, M. H., WESTERWEEL, J., ADRIAN, R. J., FRIEDRICH, R. & NIEUWSTADT, F. T. M. 1994 Fully developed turbulent pipe flow: a comparison between direct numerical simulation and experiment. *J. Fluid Mech.* **268**, 175–209.

GAVRILOV, A. A. & RUDYAK, V. YA. 2016 Direct numerical simulation of the turbulent flows of power-law fluids in a circular pipe. *Thermophys. Aeromech.* **23** (4), 473–486.

GNAMBODE, P. S., ORLANDI, P., OULD-ROUISS, M. & NICOLAS, X. 2015 Large-eddy simulation of turbulent pipe flow of power-law fluids. *Intl J. Heat Fluid Flow* **54**, 196–210.

GUERMOND, J. L., MINEV, P. & SHEN, J. 2006 An overview of projection methods for incompressible flows. *Comput. Meth. Appl. Mech. Engng* **195**, 6011–6045.

GUZEL, B., FRIGAARD, I. & MARTINEZ, D. M. 2009 Predicting laminar turbulent transition in Poiseuille pipe flow for non-Newtonian fluids. *Chem. Engng Sci.* **64** (2), 254–264.

HARTNETT, J. P. & KOSTIC, M. 1990 Turbulent friction factor correlations for power law fluids in circular and non-circular channels. *Intl Commun. Heat Mass Transfer* **17** (1), 59–65.

HUTCHINS, N & MARUSIC, IVAN 2007 Evidence of very long meandering features in the logarithmic region of turbulent boundary layers. *J. Fluid Mech.* **579**, 1–28.

KARNIADAKIS, G. E., ISRAELI, M. & ORSZAG, S. A. 1991 High-order splitting methods for the incompressible Navier–Stokes equations. *J. Comput. Phys.* **97** (2), 414–443.

LESLIE, D. C. & GAO, S. 1988 The stability of spectral schemes for the large eddy simulation of channel flows. *Intl J. Numer. Meth. Fluids* **8** (9), 1107–1116.

MADLENER, K., FREY, B. & CIEZKI, H. K. 2009 Generalized Reynolds number for non-Newtonian fluids. *Progr. Propul. Phys.* **1**, 237–250.

MALIN, M. R. 1997 Turbulent pipe flow of power-law fluids. *Intl Commun. Heat Mass Transfer* **24**, 977–988.

METZNER, A. B. & REED, J. C. 1955 Flow of non-Newtonian fluids – correlations for laminar, transition and turbulent flow regimes. *AIChE J.* **1**, 434–444.

MOSER, R. D., KIM, J. & MANSOUR, N. N. 1999 Direct numerical simulation of turbulent channel flow up to $re_\tau = 590$. *Phys. Fluids* **11** (4), 943–945.

OHTA, T. & MIYASHITA, M. 2014 DNS and LES with an extended Smagorinsky model for wall turbulence in non-Newtonian viscous fluids. *J. Non-Newtonian Fluid Mech.* **206**, 29–39.

PINHO, F. T. 2003 A GNF framework for turbulent flow models of drag-reducing fluids and a proposal for a k–ε type closure. *J. Non-Newtonian Fluid Mech.* **114**, 149–184.

PINHO, F. T. & WHITELAW, J. H. 1990 Flow of non-Newtonian fluids in a pipe. *J. Non-Newtonian Fluid Mech.* **34**, 129–144.

PIOMELLI, U. 1997 Large-eddy simulations: where we stand. In *Advances in DNS/LES* (ed. C. Liu & Z. Liu), pp. 93–104. AFOSR.

POPE, S. B 2000 *Turbulent Flows*. Cambridge University Press.

PTASINSKI, P. K., BOERSMA, B. J., NIEUWSTADT, F. T. M., HULSEN, M. A., VAN DEN BRULE, B. H. A. A. & HUNT, J. C. R. 2003 Turbulent channel flow near maximum drag reduction: simulations, experiments and mechanisms. *J. Fluid Mech.* **490**, 251–291.

PTASINSKI, P. K., NIEUWSTADT, F. T. M., VAN DEN BRULE, B. H. A. A. & HULSEN, M. A. 2001 Experiments in turbulent pipe flow with polymer additives at maximum drag reduction. *Flow Turbul. Combust.* **66**, 159–182.

RUDMAN, M. & BLACKBURN, H. M. 2006 Direct numerical simulation of turbulent non-Newtonian flow using a spectral element method. *Appl. Math. Model* **30**, 1229–1248.

RUDMAN, M., BLACKBURN, H. M., GRAHAM, L. J. W. & PULLUM, L. 2004 Turbulent pipe flow of non-Newtonian fluids. *J. Non-Newtonian Fluid Mech.* **118** (1), 33–48.

RUDMAN, M., GRAHAM, L. J. W., BLACKBURN, H. M. & PULLUM, L. 2002 Non-Newtonian turbulent and transitional pipe flow. In *15th Int. Conf. Hydrotransport*, pp. 271–286. BHR Group.

SINGH, J., RUDMAN, M., BLACKBURN, H. M., CHRYSS, A., PULLUM, L. & GRAHAH, L. J. W. 2016 The importance of rheology characterization in predicting turbulent pipe flow of generalized Newtonian fluids. *J. Non-Newtonian Fluid Mech.* **232**, 11–21.

SLATTER, P. T. & LAZARUS, J. H. 1993 Critical flow in slurry pipeline. In *12th Int. Conf. on Slurry Handling and Pipeline Transport, Hydrotransport 12*, pp. 639–658. BHRG Fluid Engineering, Cranfield.

THAIS, L., GATSKI, T. B. & MOMPEAN, G. 2013 Analysis of polymer drag reduction mechanisms from energy budgets. *Intl J. Heat Fluid Flow* **43**, 52–61.

TOMITA, Y. 1959 A study of non-Newtonian flow in pipe lines. *Bull. JSME* **2** (5), 10–16.

DEN TOONDER, J. M. J. & NIEUWSTADT, F. T. M. 1997 Reynolds number effects in a turbulent pipe flow for low to moderate *Re*. *Phys. Fluids* **9** (11), 3398–3409.

WALLACE, J. M. 2016 Quadrant analysis in turbulence research: history and evolution. *Annu. Rev. Fluid Mech.* **48** (1), 131–158.

WALLACE, J. M., ECKELMANN, H. & BRODKEY, R. S. 1972 The wall region in turbulent shear flow. *J. Fluid Mech.* **54** (01), 39–48.

WILSON, K. C. & THOMAS, A. D. 1985 A new analysis of the turbulent flow of non-Newtonian fluids. *Can. J. Chem. Engng* **63**, 539–546.